

## **Article**

Cite this article: Hill T. Flowers GE. Bingham D, Hoffman MJ (2025) Emulator-based Bayesian calibration of a subglacial drainage model. Annals of Glaciology 66, e22, 1-18. https://doi.org/ 10.1017/aog.2025.10016

Received: 24 December 2024 Revised: 20 May 2025 Accepted: 23 June 2025

#### **Keywords:**

Glacier hydrology; Greenland ice sheet; Ice-sheet modelling; subglacial processes

Corresponding author: Tim Hill; Email: tim\_hill\_2@sfu.ca

© The Author(s), 2025. Published by Cambridge University Press on behalf of International Glaciological Society. This is an Open Access article, distributed under the terms of the Creative Commons Attribution-NonCommercial-ShareAlike licence (http://creativecommons.org/licenses/ by-nc-sa/4.0), which permits non-commercial re-use, distribution, and reproduction in any medium, provided the same Creative Commons licence is used to distribute the re-used or adapted article and the original article is properly cited. The written permission of Cambridge University Press must be obtained prior to any commercial

# Emulator-based Bayesian calibration of a subglacial drainage model

Tim Hill<sup>1</sup> D, Gwenn E. Flowers<sup>1</sup> D, Derek Bingham<sup>2</sup> and Matthew J. Hoffman<sup>3</sup> D



<sup>1</sup>Department of Earth Sciences, Simon Fraser University, Burnaby, BC, Canada; <sup>2</sup>Department of Statistics and Actuarial Science, Simon Fraser University, Burnaby, BC, Canada and <sup>3</sup>Fluid Dynamics and Solid Mechanics Group, Los Alamos National Laboratory, Los Alamos, NM, USA

#### **Abstract**

Subglacial drainage models, often motivated by the relationship between hydrology and ice flow, sensitively depend on numerous unconstrained parameters. We explore using borehole waterpressure time series to calibrate the uncertain parameters of a popular subglacial drainage model, taking a Bayesian perspective to quantify the uncertainty in parameter estimates and in the calibrated model predictions. To reduce the computation time associated with Markov Chain Monte Carlo sampling, we construct a fast Gaussian process emulator to stand in for the subglacial drainage model. We first carry out a calibration experiment using synthetic observations consisting of model simulations with hidden parameter values as a demonstration of the method. Using real borehole water pressures measured in western Greenland, we find meaningful constraints on four of the eight model parameters and a factor-of-three reduction in uncertainty of the calibrated model predictions. These experiments illustrate Gaussian process-based Bayesian inference as a useful tool for calibration and uncertainty quantification of complex glaciological models using field data. However, significant differences between the calibrated model and the borehole data suggest that structural limitations of the model, rather than poorly constrained parameters or computational cost, remain the most important constraint on subglacial drainage modelling.

#### 1. Introduction

Subglacial drainage models have numerous uncertain parameters that control their behaviour (e.g. Werder and others, 2013; Hager and others, 2022). If accurate subglacial drainage models are important in reproducing realistic ice-flow patterns as is often claimed (e.g. Khan and others, 2024; Sommers and others, 2024), it follows that well-constrained model parameters are important for well-calibrated model predictions. Such predictions should have an associated uncertainty, and the predictive skill of any calibrated model should be critically assessed.

A common strategy used to select parameter values in a subglacial drainage model is to identify 'low', 'medium' and 'high' values for a subset of influential parameters (e.g. Dow, 2022) and to sample these values with one-at-a-time (e.g. Khan and others, 2024) or, rarely, all-at-once (e.g. Hager and others, 2022) sampling. In the absence of field data, parameter values may be selected based on producing a modelled drainage system consistent with prior expectations of realistic subglacial drainage (i.e. water pressure near ice overburden, seasonal development of subglacial channels) (e.g. Werder and others, 2013). When data are available, models have been tuned based on consistency with radar specularity as a hypothesized indicator of channelized versus distributed flow (e.g. Dow and others, 2020; Hager and others, 2022), satellite-altimetryderived subglacial lake filling and drainage cycles (e.g. Wearing and others, 2024) and mapped locations of eskers and other subglacial landforms indicative of past subglacial drainage characteristics (e.g. Hepburn and others, 2024). Coupled hydrology-ice-flow models have also been tuned to match observed ice surface velocities (e.g. Ehrenfeucht and others, 2023; Khan and others, 2024).

A suite of field data has been used in inverse models to infer more about subglacial drainage properties than revealed by manual tuning. Certain parameter values, such as the roughness of ice-walled englacial conduits which plays a role in heat transfer and conduit enlargement, have been inferred from experiments with tracer dye injections into moulins (e.g. Werder and Funk, 2009) and moulin water-pressure measurements (e.g. Pohle and others, 2022). However, given the expected discrepancy between modelled and observed subglacial drainage, the parameter values that describe the real system may not produce the best model-data fit. Inverse modelling approaches have constrained subglacial channel-network characteristics such as channel radius and hydraulic gradient based on dense passive seismic measurements (e.g. Nanni and others, 2021) or a combination of borehole water-pressure time series and tracer transit times

cambridge.org/aog



(e.g. Irarrazaval and others, 2019, 2021). Based on a dense borehole array, Rada Giacaman and Schoof 2023 characterized a spectrum of seasonal water-pressure patterns.

Formal model calibration and uncertainty quantification (e.g. Kennedy and O'Hagan, 2001; Higdon and others, 2004), based on evaluating the misfit between model outputs and actual data over the entire space of plausible parameter values, provides a path forward for constraining the values of all influential model parameters and determining the corresponding best model predictions with associated uncertainty. Formal calibration of subglacial drainage model parameters has rarely been attempted. For instance, Irarrazaval and others (2019, 2021) inferred the posterior distributions of channel network characteristics and hydraulic transmissivity by using a simplified, steady-state forward hydrology model to enable Bayesian inference. In the coupled hydrology-dynamics setting, calibration has been carried out by comparing modelled and satellite-derived annual average ice surface speed (Brinkerhoff and others, 2021).

In a previous study (Hill and others, 2025), we constructed a Gaussian process emulator (e.g. Higdon and others, 2008) of the Glacier Drainage System (GlaDS) subglacial drainage model (Werder and others, 2013) that accelerates modelling by three orders of magnitude. In this study, we combine the Gaussian process emulator with borehole observations from western Greenland (Meierbachtol and others, 2013; Wright and others, 2016) to explore the possibility of more directly constraining subglacial drainage model parameters. Using Bayesian inference (e.g, Higdon and others, 2004; Gelman and others, 2013), we infer distributions of the eight most-uncertain GlaDS model parameters along with the corresponding uncertainty in calibrated model outputs. We first carry out a calibration experiment using a synthetic, model-generated water-pressure time series to quantify the performance and benefits of the emulator-based Bayesian calibration approach. Then, using real borehole water-pressure data, we derive calibrated, probabilistic estimates of parameter values and corresponding calibrated model predictions, and assess the remaining uncertainty and discrepancy in drainage-system characteristics to identify performance-limiting issues.

## 2. Real and synthetic water-pressure time series

The calibration experiments are carried out on a  $\sim 13\,000\,\mathrm{km}^2$  catchment in the Kangerlussuaq sector of western Greenland that includes Isunnguata Sermia (IS), Russell Glacier (RG) and Leverett Glacier (LG) basins (Fig. 1). This well-studied portion of the ice sheet has been used extensively for in situ and modelling studies of Greenland hydrology (e.g. Bartholomew and others, 2011; Sole and others, 2013; Lindbäck and others, 2015; Derkacheva and others, 2021; Harper and others, 2021), including previous emulator-based subglacial drainage modelling (Brinkerhoff and others, 2021; Verjans and Robel, 2024). Importantly, this sector of west Greenland has a suite of borehole time series data, including basal water pressure, obtained along a transect from near the margin up to 46 km inland spanning 2010–15 (see Table 1 from Wright and others, 2016).

## 2.1. Borehole water-pressure data

We use hydraulic head measurements from a drilling campaign described in Meierbachtol and others 2013 and summarized by Wright and others 2016. Over the 2010–15 period, a total of 32 boreholes were drilled to the bed, with 14 of these boreholes

measuring basal water pressure. The majority of the boreholes where water pressure was measured were inferred to have intersected hydraulically isolated basal cavities (e.g. Meierbachtol and others, 2016). Since the subglacial drainage model is a continuum model that assumes hydraulically connected drainage across the domain, we select a single water-pressure time series from a borehole  $\sim$ 27 km from the margin (67.204° N, 49.718° W; Fig. 1c), denoted GL12-2A, as the only time series representing hydraulically connected drainage and that includes data from within and outside of the melt season (Fig. 1e). This borehole intersects a bed trough approximately 3 km across and 200 m deep, where the ice thickness is 695.5 m as measured with the drilling hose (Wright and others, 2016). Hydraulic head values are converted into a fraction of overburden using the reported ice thickness and assuming an ice density  $\rho_{\rm i}=910\,{\rm kg\,m^{-3}}$  (Wright and others, 2016). The flotation fraction time series spans 16 June 2012 to 24 July 2013, and we use the data from the beginning of the record only until the end of 2012 for calibration since the data quality degrades the longer the instruments are deployed (personal communication from J. Harper, 2024). We compute the daily mean of the  $\sim 15$ -min data for comparison with model outputs.

#### 2.2. Synthetic water-pressure data

We carry out a synthetic calibration experiment on the domain described above as a methodological example and to derive an upper bound on the strength of constraints that could be learned from point-scale water-pressure time series. Since there will be irreducible discrepancy between the model output and real borehole data, the real calibration experiment is expected to produce weaker constraints. The synthetic water-pressure data consist of modelled water pressure (as described in Section 3) using hidden parameter values, and the goal of the experiment is to assess the accuracy and uncertainty in inferred values. We use outputs chosen from a simulation that has high winter water pressure and low summer water pressure relative to the median simulation (Fig. 1d), since subglacial drainage models commonly underestimate winter water pressure relative to observations (e.g. Downs and others, 2018).

## 3. Forward model

#### 3.1. Subglacial drainage model

We use the GlaDS model (Werder and others, 2013) as the physically based forward model of subglacial drainage. GlaDS represents interacting distributed and channelized drainage systems. Distributed drainage is modelled as macroporous sheet flow and is intended to represent area-averaged flow through a network of hydraulically connected cavities formed in the lee of bed obstacles. Sheet flow transitions between laminar and turbulent regimes depending on the local Reynolds number (Hill and others, 2024). Channelized drainage is modelled as a network of onedimensional channels melted into the ice (Röthlisberger, 1972), numerically located on the edges of mesh elements. The model does not represent hydraulically isolated or weakly connected drainage (e.g. Murray and Clarke, 1995; Andrews and others, 2014), which has been shown to play an important role in relating borehole water-pressure time series to surface-velocity observations (Hoffman and others, 2016). We have therefore selected the borehole water-pressure record (as described above) that appears to best represent hydraulically connected drainage.

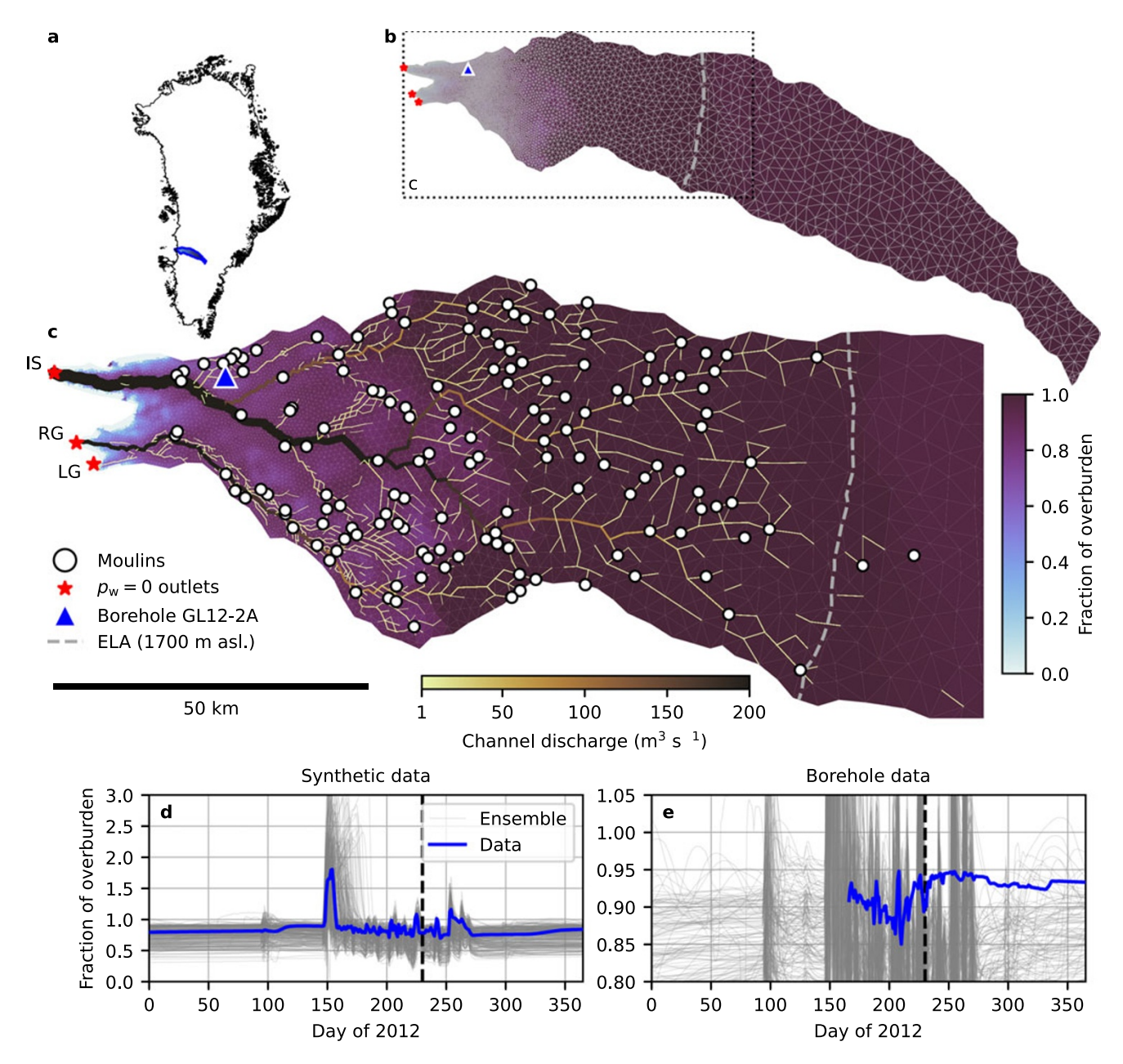


Figure 1. Greenland numerical domain and calibration data. (a) Study area within Greenland Ice Sheet. (b) Numerical mesh and flotation fraction for an example model output with approximate equilibrium line altitude sketched as dashed line (Smeets and others, 2018). (c) Example flotation fraction and channel discharge for the area below 1850 m a.s.l. with moulin positions from Yang and Smith 2016 and location of in situ borehole water-pressure data (Meierbachtol and others, 2013; Wright and others, 2016) shown as a blue triangle. Atmospheric pressure ( $p_{\rm w}=0$ ) outlet nodes for Isunnguata Sermia (IS), Russell Glacier (RG) and Leverett Glacier (LG) are shown as red stars. (d) Ensemble of GlaDS-simulated flotation-fraction values and synthetic data. (e) Ensemble of GlaDS-simulated flotation-fraction values and in situ borehole data (Meierbachtol and others, 2013; Wright and others, 2016). Vertical dashed line in (d, e) corresponds to the day shown in (b, c).

GlaDS requires specification of several poorly constrained parameters. We consider eight parameters,  $[k_s, k_c, h_b, r_b, A, l_c, \omega, e_v]$  (defined in Table 1), as the uncertain parameters to be calibrated. These parameters control the transmissivity of the drainage system  $(k_s, k_c)$ , the geometry of subglacial cavities  $(h_b, r_b)$ , the material rheology of the basal ice layer (A), the width of sheet flow that contributes to channelization  $(l_c)$ , the bulk Reynolds number at which sheet-flow transitions from laminar to turbulent  $(\omega)$  and the englacial void fraction available for transient water storage  $(e_v)$ . One could in

principle consider the channel-flow exponents  $\alpha_c = 5/4$  and  $\beta_c = 3/2$  as uncertain calibration parameters as well. However, we assume flow in R-channels is well-described by turbulent Darcy–Weisbach flow  $Q = -k_c S^{\alpha_c} \left| \frac{\partial \phi_c}{\partial x} \right|^{\beta_c-2} \frac{\partial \phi_c}{\partial x}$  (Werder and others, 2013) for discharge Q, channel area S, hydraulic potential  $\phi$  and along-channel coordinate x and keep these parameters fixed. Other model parameters are physical constants, so we consider this to be a comprehensive assessment of parametric uncertainty, conditioned on the turbulent-channel assumption.

**Table 1.** Constants (top group), fixed model parameters for GlaDS simulations (middle group) and model parameters and ranges used for training the Gaussian process emulator and inference (bottom group). The basal speed  $u_{\rm b}$  and basal melt rate  $\dot{m}_{\rm s}$  are fixed, spatially varying fields, with bracketed values indicating the minimum and maximum

	Parameter	Value	Units
$ ho_{w}$	Density of water	1000	$kg m^{-3}$
$ ho_{i}$	Density of ice	910	$kg  m^{-3}$
g	Gravitational	9.81	${ m m~s^{-2}}$
	acceleration		_
L	Latent heat of fusion	$3.34 \times 10^{5}$	$\rm Jkg^{-1}$
$c_{\rm w}$	Specific heat capacity of water	$4.22\times10^3$	$J kg^{-1}$
$c_{\rm t}$	Pressure melting coefficient	$-7.50 \times 10^{-8}$	$\mathrm{K}\mathrm{Pa}^{-1}$
$\nu$	Kinematic viscosity of water at 0°C	$1.793 \times 10^{-6}$	$\mathrm{m}^2\mathrm{s}^{-1}$
$\alpha_{c}$	Channel-flow exponent	5/4	-
$\beta_{c}$	Channel-flow exponent	3/2	-
$u_{\rm b}$	Basal speed	[0.11, 52]	${ m m~a^{-1}}$
n	Ice-flow exponent	3	-
$\dot{m}_{\rm s}$	Basal melt rate	[0.0026, 0.043]	$m \text{ w.e. } a^{-1}$
$k_{\rm s}$	Sheet conductivity	[0.001, 0.1]	$\mathrm{Pa}\mathrm{s}^{-1}$
$k_{\rm c}$	Channel conductivity	[0.1, 1.0]	$ m m^{3/2}  s^{-1}$
$h_{\rm b}$	Bed bump height	[0.05, 1]	m
$r_{\rm b}$	Bed bump aspect ratio	[10, 100]	-
Α	Ice flow-law coefficient	$[10^{-24}, 10^{-22}]$	$Pa^{-3} s^{-1}$
$l_{\rm c}$	Width of sheet beneath	[1, 100]	m
	channels	[1/500 1/5000]	
$\omega$	Laminar-turbulent	[1/500, 1/5000]	-
$e_{ m v}$	transition parameter Englacial void fraction	$[10^{-4}, 10^{-3}]$	_

#### 3.2. Model domain and discretization

The model domain is defined as a subglacial hydraulic catchment for the three proglacial outlets identified in Figure 1. These outlets correspond to the Isortoq River (for the IS sub-catchment) and two branches of the Sandflugtsdalen River (for the RG and LG sub-catchments) (fig. 1 from Lindbäck and others, 2015). The hydraulic catchment outline is defined by assuming water pressure is equal to ice overburden,  $p_{\rm w}=\rho_1 gH$ , using 150 m-resolution IceBridge BedMachine Greenland (Morlighem and others, 2017, 2022) for surface elevation, bed elevation and the land–ice mask. The numerical domain consists of a triangular mesh with 4897 nodes that is refined to have edge lengths ~500 m below 1000 m a.s.l. and as large as 5000 m above 2000 m a.s.l. (Fig. 1). For calibration and to generate synthetic data (Section 2.2), we extract modelled values at a single node near the borehole that was chosen to be most representative of observed conditions (Figs S1 and S2).

## 3.3. Melt and basal velocity forcing

We force GlaDS with daily surface melt and steady basal melt fields. Surface melt rates consist of daily mean 5.5 km-resolution RACMO2.3p2 (Noël and others, 2018) surface runoff outputs for 2010–13. Meltwater is routed to the bed through 148 moulins previously mapped by Yang and Smith 2016, with meltwater instantaneously accumulated within sub-catchments defined as Voronoi diagrams centred on each moulin. Basal melt rates are prescribed as the sum of melt rates from time-invariant geothermal and frictional heat fluxes. The geothermal flux linearly varies between  $27 \, \mathrm{mW} \, \mathrm{m}^{-2}$  at the margin and  $49 \, \mathrm{mW} \, \mathrm{m}^{-2}$  at the ice divide based on borehole observations (Meierbachtol and others, 2015). The frictional heat flux from sliding is computed as  $u_b \tau_b$  for basal

speed  $u_{\rm b}$  and basal drag  $\tau_{\rm b}$ . We assume that basal speed  $u_{\rm b}$ , basal drag and therefore frictional heat flux, are constant in time while acknowledging that substantial seasonal melt-forced velocity variations are observed in this region (e.g. van de Wal and others, 2008; Derkacheva and others, 2021). Basal drag is approximated as equal to the driving stress,  $\tau_{\rm b} = \rho_i g H |\nabla z_{\rm s}|$ , where  $z_{\rm s}$  is the surface elevation. Basal velocity is estimated as a uniform fraction of MEaSUREs multi-year (1995–2015) average surface velocities (Joughin and others, 2016, 2018) by computing the ratio (0.33) that results in a maximum frictional-melt rate of 4 cm w.e. a<sup>-1</sup> to match maximum frictional-melt rates derived from borehole data and satellite observations (Harper and others, 2021).

We use daily average melt forcing and borehole water pressures, rather than resolving diurnal variations, to calibrate the drainage model because of the difficulty the model has in reproducing realistic diurnal variations and the challenge of constructing reasonably realistic sub-daily resolution melt inputs to drive the drainage model. When forced with diurnally varying melt inputs, GlaDS tends to produce muted variations over 24 hour periods, with larger variations on multi-day timescales (e.g. Hill and others, 2024). This incorrect spectral response is opposite to that shown by the borehole time series, which has variations in the baseline water pressure on the order of 5% of overburden, with diurnal variations up to 15% of overburden. Perhaps because the model does not produce strong diurnal variations, the model predicts minimal differences in drainage system evolution between daily and sub-daily forcing (Werder and others, 2013).

#### 3.4. Boundary and initial conditions

No-flux subglacial drainage conditions are prescribed everywhere along the boundary, except at the three proglacial outlets where we prescribe zero water pressure. The outflow nodes are chosen as the nodes with locally minimum hydraulic potential, assuming water pressure equal to ice overburden, near the prescribed outlets used to define the hydraulic catchment (Fig. 1). We do not include an outflow node for the Point 660 catchment between the IS and RG catchments (Lindbäck and others, 2015) since we do not find a clear hydraulic potential minimum in this location. The model is initialized with no channels, water pressure equal to ice overburden and water layer thickness equal to 20% of the bed bump height. We run the model from 2010 until the end of 2012 and discard the first 2 years (2010–11) as a spin-up period to bring the model into a quasi-periodic state (e.g. Ehrenfeucht and others, 2023; Sommers and others, 2024).

## 3.5. Numerics

For the large ensemble of GlaDS simulations (Section 4.3), we have found that it is necessary to use a  $0.2\,\mathrm{h}$  timestep and a solver residual tolerance of  $10^{-5}$ . This timestep is short compared to the daily melt-forcing frequency, and the  $10^{-5}$  solver tolerance is smaller than often used for more typical GlaDS simulations. Using numerical parameters that are less strict results in noticeable changes in modelled water pressure for certain simulations in the ensemble (Fig. S16). Since we are purposely running GlaDS with unusual parameter values as part of the large ensemble, it is not unexpected that we need to be cautious in selecting numerical parameters to ensure that model runs are appropriately converged. We have also found that using simulations with numerical artefacts results in an emulator with high prediction error and parameter estimates that are inconsistent with the true parameter values in the synthetic

calibration experiment since the simulation outputs do not change predictably with respect to model parameters. With these numerical parameters, each GlaDS simulation takes  $\sim$ 8.75 hours on a single AMD Rome 7532 CPU and requires  $\sim$ 1 GB of memory.

#### 4. Inverse model

#### 4.1. Bayesian inference

Given time series observations of subglacial water pressure, we aim to estimate the GlaDS parameter values that produce modelled water pressure consistent with the observations. Model–data fit is assessed by the sum-of-squares error between the observed time series and the modelled time series extracted at the node nearest to the borehole location. We use Bayesian inference to estimate probability distributions of GlaDS parameter values that minimize model–data squared error.

Let  $y \in \mathbb{R}^{n_t}$  be the standardized observations, consisting of a number  $n_t$  days of flotation fraction values. The observations y are standardized by subtracting the mean and dividing by the standard deviation of the simulation ensemble (Section 4.3). Consistent with previous work (e.g. Brinkerhoff and others, 2021), we apply a log-transform to the model parameters and standardize the log-parameters such that they fall in the interval [0,1]. We denote the vector of log-standardized GlaDS parameters  $t \in [0,1]^d$ , where d=8 is the number of calibration model parameters. With F(t) the standardized (i.e. centred and scaled by the simulation mean and standard deviation) forward model (GlaDS) evaluated for log-standardized parameter values t, we model the observations as being generated from the forward model evaluated for some unknown calibration parameter values  $t = \theta$ ,

$$y = F(\theta) + \epsilon_{\nu}. \tag{1}$$

The observation error  $\epsilon_y \sim \mathcal{N}(\mathbf{0}, \Sigma_y)$  is modelled as multivariate normal with zero mean and covariance  $\Sigma_y = \lambda_y^{-1}\mathbf{I}$  parameterized by precision  $\lambda_y$ . That is, we assume that the observations  $\mathbf{y}$  are multivariate normally distributed with mean given by the standardized forward model evaluated for the unknown calibration parameters  $F(\boldsymbol{\theta})$  and with covariance  $\Sigma_y$ :  $\mathbf{y} \sim \mathcal{N}(F(\boldsymbol{\theta}), \Sigma_y)$ .

From Bayes' theorem, the distribution of the model parameters  $\theta$  given the data, also called the posterior distribution, is

$$P(\theta|\mathbf{y}) \propto P(\mathbf{y}|\theta)P(\theta).$$
 (2)

The first term on the right-hand-side,  $P(y|\theta)$ , called the likelihood, is the probability of sampling the data y from the model (1) given certain GlaDS parameters  $\theta$  and represents model–data fit. For normally distributed errors, model-data fit is quantified by the squared error. The second term,  $P(\theta)$ , called the prior distribution, specifies our prior belief about the value of  $\theta$ . Equation (2) indicates that we should update our belief in the calibration parameter values  $\theta$  in light of the data y in order to reduce the squared error between the model and data. By maximizing the posterior probability (Eqn (2)), we minimize model-data misfit, with the prior distributions taking the place of regularization terms. As is common for Bayesian inference (e.g. Higdon and others, 2004; Gelman and others, 2013), we approximate the posterior distribution by iteratively sampling from the posterior distribution with Metropolis-Hastings Markov Chain Monte Carlo (MCMC; Metropolis and others, 1953; Gattiker and others, 2020). However, each likelihood evaluation  $P(y|\theta)$  involves running a forward GlaDS simulation. For the GlaDS model as used here, which

**Table 2.** Prior distributions on log-standardized subglacial drainage model parameters and Gaussian process hyperparameters. Uniform distributions U(a,b) are parameterized by the interval [a,b]. Gamma distributions  $\Gamma(a,b)$  are parameterized by the shape parameter a and the rate parameter b such that the mean is  $\frac{a}{1}$ .

	Parameter	Distribution
$\overline{\theta}$	Standardized GlaDS parameters	U(0,1)
$\lambda_{v}$	Observation precision	$\Gamma(5,5)$
$\lambda_{\eta}^{'}$	Simulation precision	$\Gamma(a_{\eta}, b_{\eta})$
$\lambda_w$	Gaussian process precision	$\Gamma(5,5)$
$\boldsymbol{\beta}$	Gaussian process input sensitivity	$\Gamma(5,5)$
$\lambda_n$	Gaussian process nugget precision	$\Gamma(3, 0.003)$

takes  $\sim$ 9 hours to run, sampling from the posterior (Eqn (2)) is intractable since the Metropolis–Hastings algorithm often requires thousands of sequential iterations to approximate the posterior distribution. To avoid this complication, we construct an emulator to stand in for GlaDS (e.g. Higdon and others, 2004; Brinkerhoff and others, 2021).

#### 4.2. Gaussian process emulator

Based on an ensemble of simulations with the forward model (GlaDS), the emulator estimates the simulated values for untested parameter values. We use a Gaussian process (GP) emulator that is more fully described by Hill and others 2025. Instead of emulating the full spatiotemporal model outputs, here we emulate the flotation-fraction time series for the node representing the borehole. The GP requires additional parameters, which we call 'hyperparameters', whose values must be estimated (Table 2). We denote their calibration values  $\phi$  to distinguish them from parameters of the subglacial drainage model (Table 1). Figure 2 and Algorithm S1 summarize the emulator-based calibration workflow.

Since GPs do not naturally scale to multivariate outputs such as a time series, we follow Higdon and others 2008 in simplifying the problem using a principal component basis representation for the forward model outputs. Letting p denote the number of principal component basis vectors used in the representation, we model the standardized forward model output as

$$F(t) = \sum_{j=1}^{p} k_j w_j(t, \phi) + \epsilon_{\eta},$$
 (3)

where  $\mathbf{k}_j$   $(1 \leq j \leq p)$  are the principal component basis vectors and  $w_j$   $(1 \leq j \leq p)$  are independent GPs. For convenience, we refer to the first term as the emulator  $\eta(\mathbf{t}, \phi) = \sum_{j=1}^p \mathbf{k}_j w_j(\mathbf{t}, \phi)$ . The error term  $\epsilon_{\eta} \sim \mathcal{N}(\mathbf{0}, \lambda_{\eta}^{-1}\mathbf{I})$ , represents basis truncation error and is parameterized by the emulator precision  $\lambda_{\eta}$ . The number of principal components p that are retained is an important choice as it influences the fidelity of the emulator predictions. We will select the number of principal components for each application by considering the proportion of variance in the simulation ensemble that is explained, the truncation error and by inspecting the residuals in the basis representation. Full details of the consequences of the basis representation, including an expression for the likelihood  $P(\mathbf{y}|\boldsymbol{\theta}, \phi)$ , are presented by Higdon and others 2008.

Each individual GP  $w_j$  is specified by its mean and covariance model. We use zero-mean GPs with a squared-exponential covariance function,

$$k_j(\mathbf{t}, \mathbf{t}') = \frac{1}{\lambda_{w,j}} \exp\left(-\sum_{i=1}^d \beta_{ij} (t_i - t_i')^2\right), \tag{4}$$

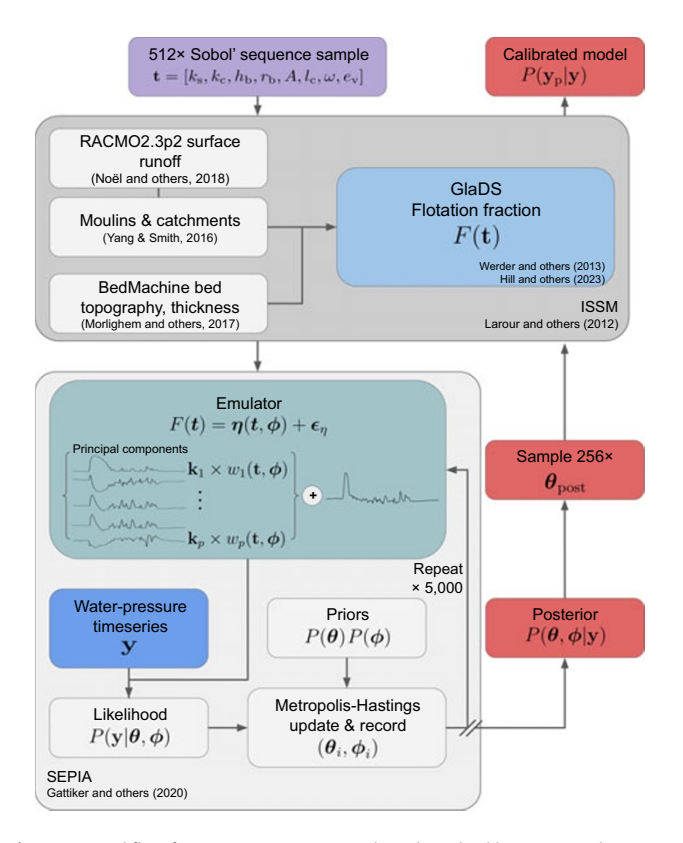


**Figure 2.** Workflow for Gaussian process emulator-based calibration.  ${\bf t}$  is the vector of log-standardized model parameters, with  ${\bf t}={\boldsymbol \theta}$  the calibration parameters that best fit the data  ${\bf y}$ , and F(t) is the modelled time series of water pressure (expressed here as flotation fraction) corresponding to log-parameters  ${\bf t}$ . The emulator  ${\boldsymbol \eta}$ , with hyperparameters  ${\boldsymbol \phi}$ , is constructed as a linear combination of p principal component basis vectors  ${\bf k}_j$  and independent scalar emulators  $w_j$  for  $j=1,\ldots,p$ . Uncertainty in the calibrated model is estimated by Monte Carlo sampling from the posterior parameter distribution.

where  $\lambda_{w,j}$  is the marginal precision (inverse variance) of the GP  $w_j$  and the  $\beta_{ij}$  ( $i=1,\ldots,d$ ) hyperparameters control the strength of dependence on each of the inputs. In practice, a small additional diagonal covariance matrix parameterized by precision  $\lambda_n$  ( $\mathcal{O}(10^3)$ ), sometimes called a nugget, is added to each GP covariance matrix to improve the numerical conditioning of the matrix. The complete hyperparameter vector, accounting for the p separate values for the GP marginal precision  $\lambda_w$ , input sensitivity  $\beta$  and nugget  $\lambda_n$ , is  $\phi = [\lambda_y, \lambda_\eta, \lambda_w, \beta, \lambda_n]$ .

We sample from the joint posterior distribution,

$$P(\theta, \phi | \mathbf{y}) \propto P(\mathbf{y} | \theta, \phi) P(\theta) P(\phi),$$
 (5)

which accounts for the uncertainty in the data *y* (Eqn (1)) as well as the replacement of the forward model with the GP emulator. We use the SEPIA package (Gattiker and others, 2020) v1.1 to construct the emulators and carry out Metropolis–Hastings sampling. Choices for the prior distributions are discussed in Section 4.3. The foundation in uncertainty quantification is a primary benefit of GP modelling compared to other deterministic options for the emulator. In particular, the addition of the emulator uncertainty to the observation uncertainty in defining the GP likelihood (Higdon and others, 2008) means that uncertainty in GP predictions is accounted for in inferring distributions of the model parameters. If the emulator has large uncertainty relative to the observational uncertainty, then the resulting posterior parameter

distributions will be noticeably wider than had we used the forward model directly (e.g. Downs and others, 2023).

#### 4.3. Ensemble design

We design the simulation ensemble to uniformly sample the log-standardized input space in order to construct an emulator with prediction performance that is approximately uniform across the log-inputs. For this, we use a Sobol' sequence (Sobol', 1967) over the logarithm of the parameters within the bounds provided in Table 1. We draw 512 samples from the Sobol' sequence, using its sequential design properties to evaluate emulator performance with power-of-2 subsets of the full sequence. We construct an independent set of inputs for testing the emulator consisting of 100 samples from a space-filling Latin hypercube design.

For parameters with a physical interpretation (e.g. the bed geometry as described by the bump height  $h_{\rm b}$  and aspect ratio  $r_{\rm b}$ , the ice-flow coefficient A and the laminar–turbulent transition parameter  $\omega$ ), we have chosen parameter ranges that encompass plausible values. For the remaining parameters, we have chosen their ranges to be reasonably wide while minimizing the number of unrealistic simulations, for example as indicated by water pressure exceeding 300% of overburden. We have found that this pressure constraint limits the lower bound of channel conductivity  $k_{\rm c}$ , sheet conductivity  $k_{\rm s}$  and englacial storage parameter  $e_{\rm v}$ .

These ranges largely encompass the values commonly used for modelling Greenland outlet glaciers with the GlaDS model (e.g. Gagliardini and Werder, 2018; Cook and others, 2020; Ehrenfeucht and others, 2023; Khan and others, 2024; Verjans and Robel, 2024; Hill and others, 2024). Some exceptions include literature values of the englacial storage parameter as low as  $e_v = 10^{-5}$  (e.g. Ehrenfeucht and others, 2023; Khan and others, 2024), channel conductivity as low as  $k_c = 0.05 \, \mathrm{m}^{3/2} \, \mathrm{s}^{-1}$  (e.g. Khan and others, 2024) and an ice-flow coefficient  $A = 2.5 \times 10^{-25} \, \mathrm{Pa}^{-3} \, \mathrm{s}^{-1}$  indicative of basal ice below the pressure-melting point (Ehrenfeucht and others, 2023). Considering the laminar–turbulent sheet-flow model, it is difficult to compare the sheet conductivity range except for studies using a laminar sheet-flow model. Gagliardini and Werder 2018 and Cook and others 2020 use a lower sheet conductivity value  $k_{\rm s} \approx 2 \times 10^{-4} \, \mathrm{Pa} \, \mathrm{s}^{-1}$ , which we have found results in peak water pressures exceeding 300% of overburden for our setup.

#### 4.4. Prior distributions

The prior distributions of GlaDS parameters  $P(\theta)$  and GP hyperparameters  $P(\phi)$  in Eqn (5) are used to express our belief in the values of these quantities. For model parameters  $\theta$ , we take a uniform U(0,1) prior distribution for the log-standardized values to express a lack of prior belief in the most likely parameter values. We use Gamma distributions  $\Gamma(a, b)$ , parameterized by shape parameter a and rate parameter b, for the hyperparameter prior distributions  $P(\phi)$  (Table 2) due to the flexibility of the  $\Gamma$  family of distributions and the fact that the probability density goes to 0 when  $\phi = 0$ . Since the inputs are scaled to the range  $t \in [0, 1]^d$ and the outputs are centred and scaled to have unit variance, we select prior distributions for the observation precision  $\lambda_{\nu}$ , GP precision  $\lambda_n$  and GP sensitivity  $\beta$  that encourage values near 1. The GP nugget  $\lambda_n$  prior distribution encourages high precision (i.e. a small nugget) with a mean of 1000 and 95% interval spanning approximately an order of magnitude. We choose the prior distribution for the simulation precision  $\lambda_n$  to express our belief that this term should account for error in the truncated principal component

basis. We choose the hyperparameters  $a=a_\eta$  and  $b=b_\eta$  to express this belief by constraining the mode to be equal to the precision of the basis representation, denoted  $\lambda_{\rm p}$ . We have found that prescribing a prior distribution that allows a wide range of simulation-precision values can sometimes result in the simulation error term  $\epsilon_\eta$  absorbing all of the variations in the output with respect to  $\theta$ , leaving the GP to revert to the mean irrespective of the given values of  $\theta$ . To express our belief that the GP should take up variations in the simulator response for different parameter values, and therefore that  $\lambda_\eta$  represents the basis truncation error, we place 95% of the probability mass of the simulation-precision prior distribution within an interval with width equal to half of the basis precision  $\lambda_{\rm p}$ . For the truncation error in synthetic and borehole calibration experiments, the prior distribution parameter values are approximately  $a_\eta \approx 100$  and  $b_\eta \approx 2$ .

#### 4.5. Posterior predictions

We produce calibrated GlaDS predictions by drawing 256 samples from the MCMC chain of GlaDS parameters (labelled  $\theta_{\rm post}$  in Fig. 2) and running the forward model (GlaDS) on the samples. Using GlaDS instead of the emulator to produce calibrated predictions allows us to investigate additional outputs such as the full spatiotemporal flotation fraction field and the distribution and extent of subglacial channels that are not predicted by the emulator.

#### 5. Results

## 5.1. Emulator performance

The performance of the emulator is evaluated by computing the root-mean-square error (RMSE) between the flotation fraction of the test GlaDS runs extracted at the borehole location and the corresponding emulator predictions. The RMSE of the emulator is relatively consistent for different choices of the number of principal components and the number of simulations in the ensemble used to train the emulator (Fig. S4), with median time-integrated RMSE between 0.064-0.088 (in units of fraction of overburden). The RMSE decreases when increasing the number of principal components from 5 to 10, with minimal change for models with more principal components. Emulator performance improves for larger training ensembles, but with differences in the median performance remaining within the interquartile range. In other words, GP performance can be slightly improved by including more training simulations and principal components, but the error reduction is small compared to the variation in emulator error across the test set. The relatively weak sensitivity to the number of principal components and training simulations reported here is consistent with the more in-depth analysis carried out by Hill and others 2025 for a simpler synthetic application. We choose to use the full set of 512 training simulations and 15 principal components, based on the levelling off of the emulator RMSE and the principal component truncation error (Fig. S3). In this case, the first 15 principal components explain 98% of the variation of the 512-member simulation ensemble.

The accuracy of the chosen emulator varies throughout the year and across the test set. To evaluate best- and worst-case scenarios for the emulator performance, we evaluate the 5th, 50th and 95th percentile realizations (Fig. 3). Absolute emulator prediction error is highest in the spring (days  $\sim$ 150–175) and for simulations with high peak water pressure (e.g. Fig. 3a). After day  $\sim$ 175, emulator

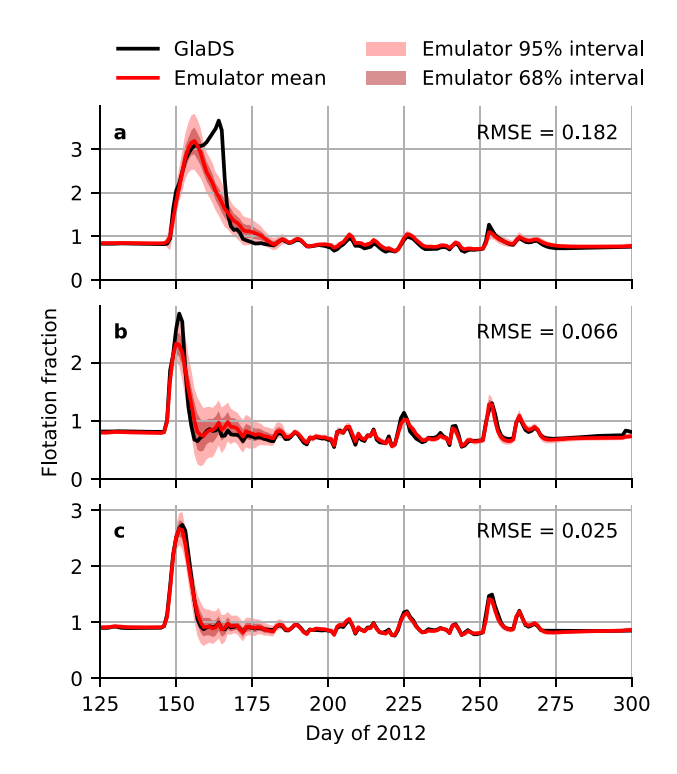


**Figure 3.** Evaluation of the Gaussian process emulator. Comparison of GlaDS simulations and emulator predictions on the test set for individual simulations with high (95th-percentile, a), median (median, b) and low (5th-percentile, c) root-mean-square-error (RMSE).

predictions capture the amplitude and duration of water-pressure variations with lower absolute error. The relative emulator error is more consistent through the year, and for some test simulations is as large through late summer as during the spring pressure peak. Winter water pressure is reproduced within a few per cent of overburden. Correspondingly, emulator predictions are most uncertain, as measured by the width of the 68% and 95% prediction intervals, between days 150–175, with uncertainty reducing to a small fraction of overburden by winter. The 95% emulator prediction intervals mostly overlap the simulated values, except in spring (Fig. 3a), indicating the emulator is appropriately estimating prediction uncertainty.

#### 5.2. Synthetic calibration experiment

For the synthetic calibration experiment, which aims to recover the true but hidden parameter values used for a reference GlaDS simulation that is labelled as data, emulator-based inference recovers the true parameter values within one standard deviation of the posterior distributions except for the sheet-channel width parameter  $l_c$  (Figs. 4 and S13). For all parameters except the laminarturbulent transition parameter  $\omega$ , the marginal posterior distributions (diagonal panels in Fig. 4) are more informative than the prior distributions. The posterior estimates of the channel conductivity  $k_{\rm c}$ , ice-flow coefficient A and the englacial storage parameter  $e_{\rm v}$ are especially well-constrained relative to their prior distributions. We have found moderate pairwise correlations, including r = 0.48between sheet conductivity  $k_s$  and the bed bump aspect ratio  $r_b$ , and r = 0.48 between  $k_c$  and A. The relatively weaker constraints on remaining parameters are consistent with a previous analysis of the sensitivity of flotation fraction to these parameters (Hill and

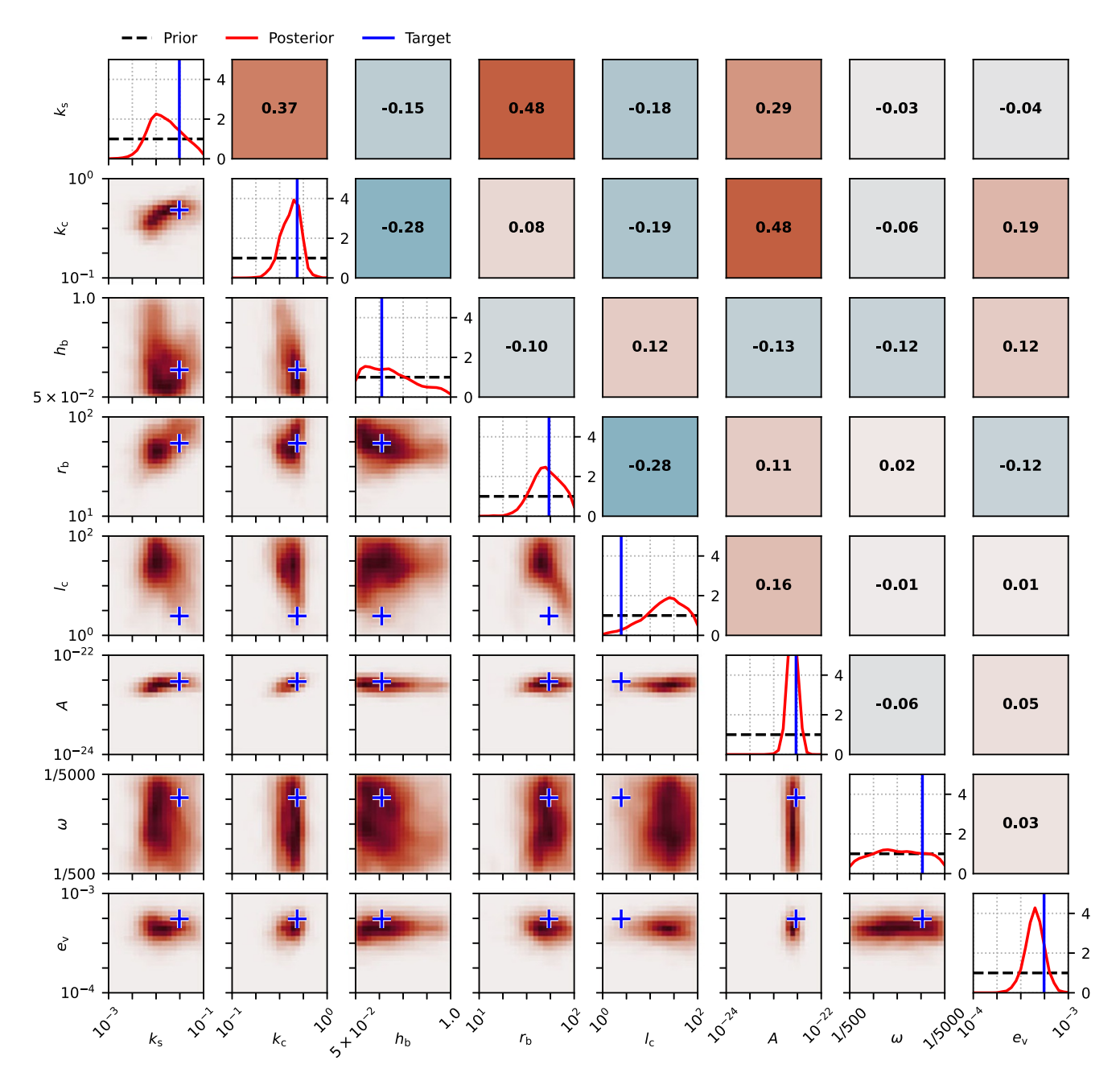


**Figure 4.** Posterior distributions  $P(\theta|y)$  using synthetic water-pressure data. Diagonal panels show marginal prior and posterior distributions along with the hidden parameter values used to generate the synthetic data. Lower left panels show pairwise joint posterior distributions and values used to generate the data as crosses. Upper right panels show the estimated pairwise Pearson correlation coefficient.

others, 2025). For  $\omega$ , the lack of sensitivity may indicate that modelled sheet-flow at the borehole location remains laminar since this area tends to become channelized early in the melt season (Hill and others, 2024)

Repeating the calibration experiment by individually considering each of the 100 test simulations as data, we consistently infer strong constraints on the value of the channel conductivity  $k_c$ , ice-flow coefficient A, englacial storage parameter  $e_v$  and the bed bump aspect ratio  $r_b$  (Fig. S14) with very little bias (Fig. S15). While we typically constrain the sheet conductivity  $k_s$ , bed bump height  $h_b$  and sheet-channel width  $l_c$  values relative to their prior distributions, the true values are more likely to be in a lower posterior probability region (Table S1).

Calibrated model predictions have a 95% prediction interval that is 3.8 times narrower than that of the ensemble of simulations with parameter values sampled from the uniform priors (Fig. 5). As expected with synthetic data produced by the model, the calibrated predictions always overlap the synthetic data within the 95% prediction interval and often within the 68% interval (i.e. approximately within one standard deviation of the mean). While flotation fraction values between days  $\sim 150-200$  have been constrained relative to the prior distribution, there remains a spread of  $\sim 100\%$  of overburden in the 95% prediction intervals. However, this has been reduced from a spread of > 200% of overburden in the original ensemble. The main discrepancy between the calibrated mean and the synthetic data is during the late-season melt events near

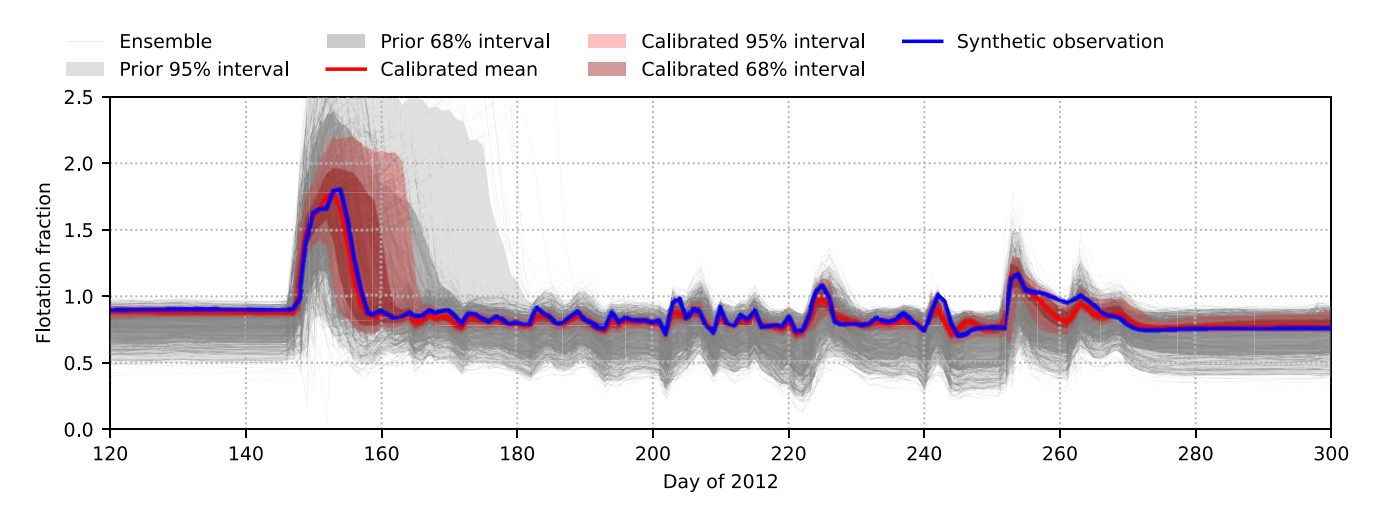


Figure 5. Comparison of prior and calibrated ensembles of GlaDS simulations using the synthetic flotation-fraction time series. The mean and prediction intervals of the calibrated model are computed by running GlaDS with 256 samples from the posterior distribution.

day 250. Perhaps as a result of the biased posterior modes, the calibrated model has a faster flotation-fraction decay between these melt events than in the synthetic data.

## 5.3. Borehole calibration experiment

For the borehole data that covers the last 199 days (16 June to 31 December) of 2012, we choose to emulate only the corresponding period of modelled water pressure, rather than modelling the entire year as was done in the synthetic calibration experiment. This simplification allows us to reduce the number of principal components used by the emulator from 15 to 12 while still explaining 98% of the variance of the ensemble. We continue to use the full ensemble of 512 simulations to train the emulator.

## 5.3.1. Full time series calibration

As expected, calibration using the borehole water-pressure time series from 16 June to 31 December 2012 produces wider posterior distributions than the synthetic experiment (Fig. 6). Since we use the same prior distributions and GlaDS ensemble as in the synthetic experiment, these differences reflect how informative the real observations are compared to the synthetic observations. As we found in the synthetic calibration experiment, we obtain some constraint relative to the prior distribution on each parameter except the laminar-turbulent transition parameter  $\omega$ . We obtain especially distinct posterior modes for channel conductivity  $k_c$ , the bed bump aspect ratio  $r_b$  and the ice-flow coefficient A. The bed bump height  $h_b$ , sheet-channel width  $l_c$  and englacial storage parameter  $e_v$  have indistinct modes but with a preference towards one side of their ranges. While we do resolve a posterior mode for the sheet conductivity  $k_s$ , this peak is not consistently observed for all emulator architectures (i.e. p values, Fig. S11) or when using different subsets of the simulation ensemble (Fig. S12), so we do not consider this a robust estimate. There is a moderate inverse correlation (r = -0.43) between  $k_c$  and  $l_c$ , with weaker correlations between other pairs. Compared to the synthetic experiment, even for parameters with a clear posterior mode (e.g.  $k_c$  and  $r_b$ ), the probability is nonzero across most of the range of values when using borehole data. The major exception is the ice-flow coefficient A, which has nearly zero marginal probability over most of its range except for the extreme upper end, indicating that the model is inconsistent with the borehole data for all but the highest *A* values (Section 6.1).

Calibrated model predictions (Fig. 7) highlight that, while the calibrated model sometimes aligns with the borehole time series, significant discrepancy remains between the calibrated model and the borehole time series. For instance, the coefficient of determination (the proportion of variance in the data explained by the calibrated model) is -3.2, where the negative indicates that the mean borehole flotation fraction is a better predictor than the calibrated model. For reference, the calibrated model predicts 93% of the variance in the synthetic calibration experiment. The negative coefficient of determination is a result of differences in the response to melt input variations between the calibrated model and the observations. In part, the model-data discrepancy may be a result of the borehole time series indicating a switch from connected to unconnected on day ~215 of 2012. For the whole duration of the record, the model consistently responds more strongly to increases in melt rate than the borehole water-pressure time series, rapidly increasing water pressure by 5% to >10% of overburden. For various instances, the borehole water-pressure time series shows negligible pressure variations (e.g. after day 250) or out-of-phase variations (e.g. near day 175) relative to the calibrated model. Following day ~220, the observed baseline water pressure increases by  $\sim$ 5% of overburden. This increase is not reproduced by the model for any parameter combinations, as evidenced by the intermittent lack of overlap of the model 95% prediction intervals with the observations. The borehole record unfortunately does not cover the spring speedup event associated with high modelled water pressures. The calibrated model, which is therefore relatively unconstrained in the spring, predicts unrealistically high water pressure from days ~150-165, with the mean prediction exceeding 150% of overburden and the 95% prediction interval reaching nearly 250%.

## 5.3.2. Independent summer and winter calibration

A major shortcoming of GlaDS and other similar models is that they typically produce low winter and high summer water pressures relative to measured or inferred water-pressure variations. This problem, in particular unrealistically high spring water pressure, persists in the calibrated model predictions. As one approach to improve the balance of winter and summer water pressure,

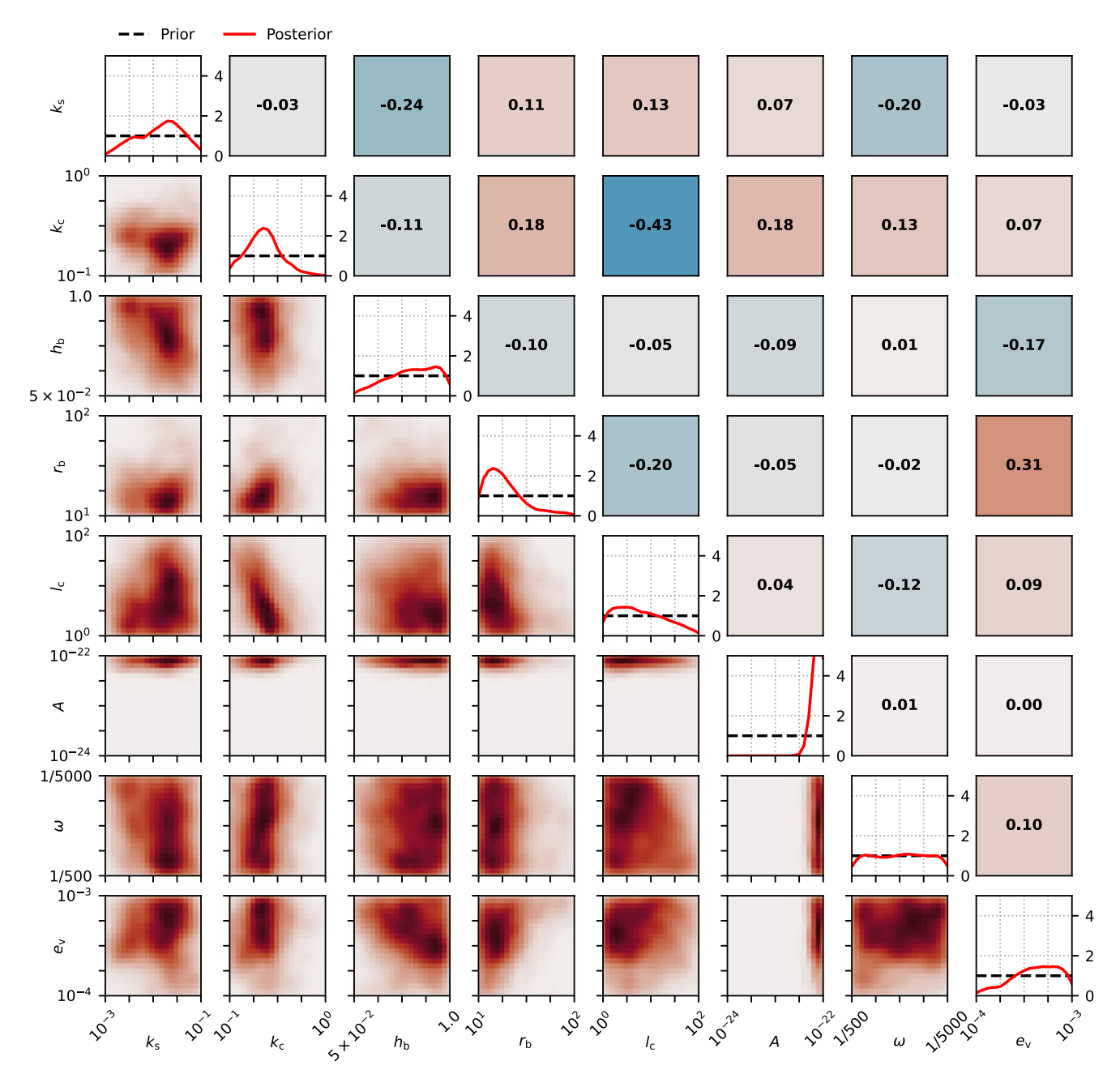


**Figure 6.** Posterior distributions  $P(\theta|y)$  using borehole flotation-fraction data. Diagonal panels show marginal prior and posterior distributions. Lower left panels show pairwise joint posterior distributions. Upper right panels show the estimated pairwise Pearson correlation coefficient.

Downs and others 2018 proposed using separate values for the sheet conductivity  $k_{\rm s}$  within and outside of the melt season. To assess the extent to which we might infer distinct parameter values for these time periods, we separately calibrate the model using subsets of the borehole time series taken within and outside of the melt season. We use within melt season data between day 166 (the beginning of the record) until day 216, when the amplitude of diurnal variations suddenly decreases (not shown), suggesting the borehole may have lost full hydraulic connectivity. Since modelled and observed flotation fraction is nearly constant through winter, the principal component decomposition does not add value in terms of describing flotation-fraction patterns (i.e. the first principal component explains  $\gg 99\%$  of the variance), and so we define

the (scalar) winter flotation fraction as the average over the last 30 days of the year.

By using different subsets of the borehole time series, we infer distinct posterior modes with overlapping distributions for the channel conductivity  $k_{\rm c}$ , bed bump aspect ratio  $r_{\rm b}$  and englacial storage parameter  $e_{\rm v}$  (Fig. 8). High values of the ice-flow coefficient A are preferred in all cases, but this preference is significantly weaker when using summer-only data. For the sheet conductivity  $k_{\rm s}$ , the strongest posterior constraint is obtained by using the full time series. We do not find differences in the most-likely sheet conductivity values by separately using winter and summer data for calibration, despite the fact that the Downs and others 2018 sheet conductivity parameterization motivated this experiment.

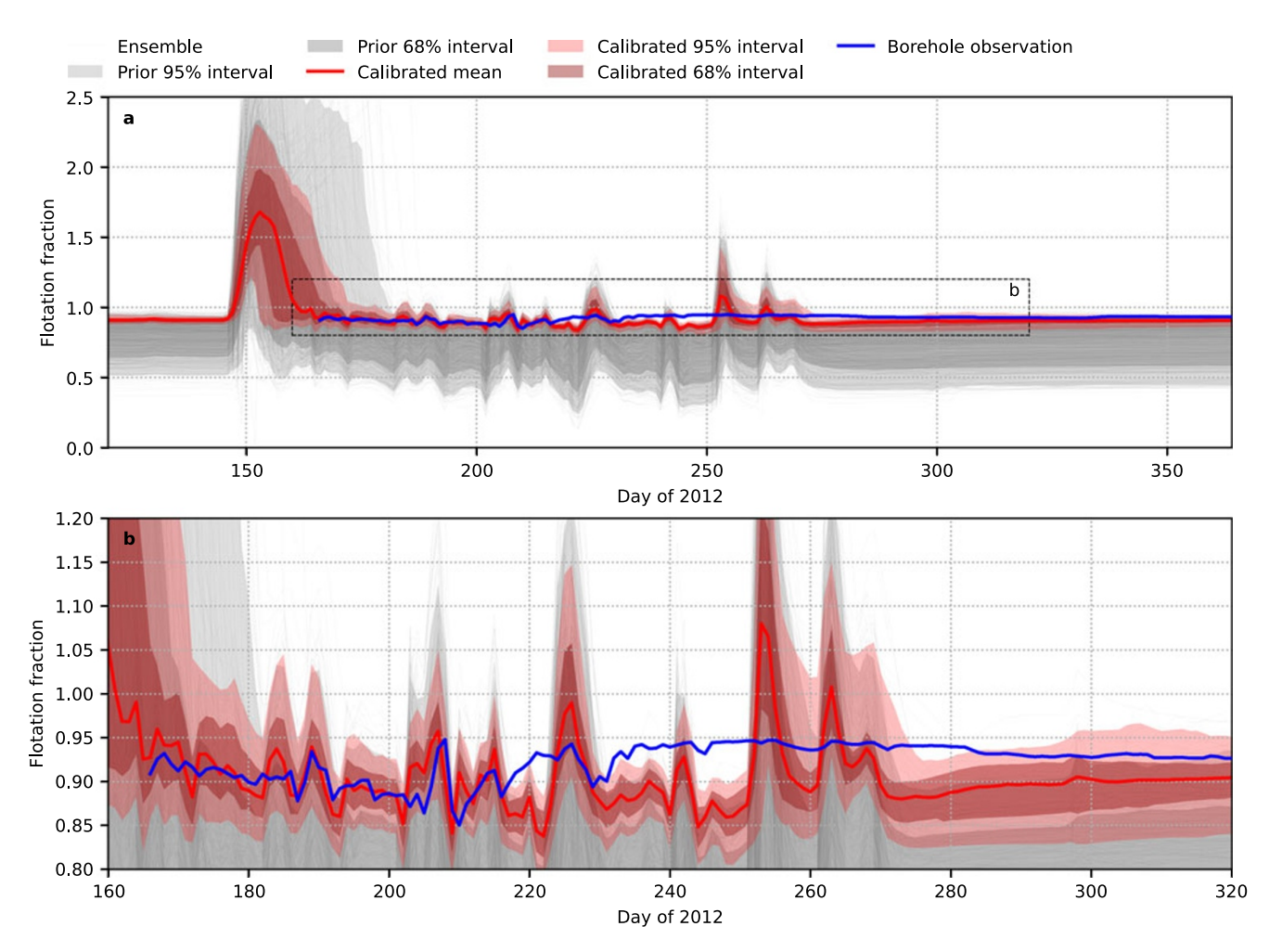


Figure 7. Comparison of prior and calibrated ensembles of GlaDS simulations using the real borehole flotation-fraction time series. The mean and prediction intervals of the calibrated model are computed by running GlaDS with 256 samples from the posterior distribution. The dashed box in (a) indicates the area shown in more detail in (b).

The distinct posterior parameter estimates for  $k_{\rm c}$  and  $r_{\rm b}$  act to increase winter water pressure and reduce summer pressure, consistent with the purpose but not the form of the sheet conductivity parameterization developed by Downs and others 2018. The englacial storage parameter  $e_{\rm v}$ , which displays posterior modes at opposite extremes of its range using winter-only data compared to summer-only and all data, does not obviously fit this pattern. The preferentially high values using summer-only and all data may be a result of the model reducing the amplitude of the pressure response to surface melt events. While we have obtained some differences in estimated parameter values by using different subsets of the borehole data, we did not find a clear and useful pattern that supports seasonally changing GlaDS parameter values.

#### 5.4. Posterior constraints on subglacial drainage system

In both synthetic and borehole experiments, the single point-scale time series reduces model uncertainty everywhere in the domain (Fig. 9). More uncertainty remains in the borehole calibration experiment, consistent with the wider spread in spring flotation-fraction predictions at the borehole location (Figs. 5 and 7). In the synthetic calibration experiment, we have approximately halved the uncertainty in the total volume of the channel network relative to the spread of the original ensemble, with a posterior distribution consistent with the volume corresponding to

the synthetic observation (Fig. 9d). In contrast, the borehole time series does not strongly constrain the volume of the channel network, but it does result in a preference towards larger channel networks than the original ensemble (Fig. 9e).

While the uncertainty in drainage system characteristics that remains after calibration with the borehole time series is larger than in the case of synthetic data, we do obtain meaningful constraints on channel network development throughout the domain and especially near the borehole location. Consistent with the channel network statistics (Fig. 9e), the model calibrated with the borehole time series shows, on average, higher channel discharge throughout the domain and especially within the IS sub-catchment (Fig. 10, see Fig. 1c for sub-catchment labels). Near the borehole, the calibrated model preferentially routes channelized flow along a consistent pathway that passes through the node used to represent the borehole. The calibrated model also has reduced flow through tributary branches which join below the borehole. Based on the difference in mean channel discharge, the borehole time series appears to provide some constraint on hydraulic potential gradients not only near the borehole but across the entire catchment.

## 5.5. Computational savings

The emulator accelerates MCMC sampling by  $\sim$ 5000 times (Table 3). This sampling density is not possible using GlaDS

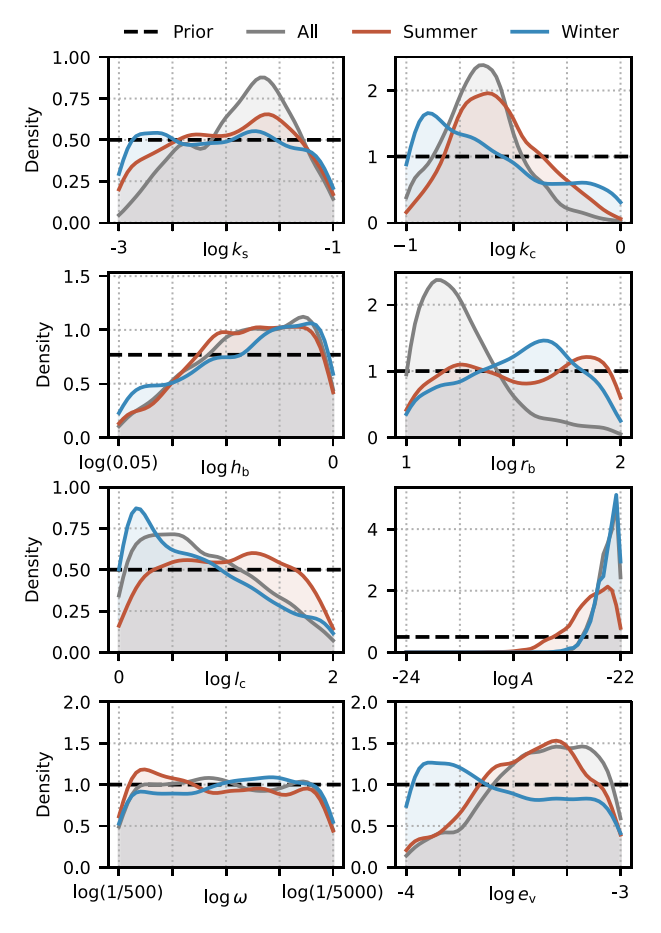


Figure 8. Comparison of marginal posterior parameter distributions using all borehole data or separately using summer and winter data.

directly. Each GlaDS simulation takes ~9 hours, and since we have used 5000 MCMC samples, drawing this many MCMC samples would take ~5 years since MCMC demands sequential evaluation. Using the GP emulator with 512 simulations and 12–15 PCs, drawing the MCMC samples takes ~6.5–8 hours. While more efficient sampling strategies are available that would require fewer samples, e.g. Metropolis-adjusted Langevin algorithm (Besag, 1994; Roberts and Tweedie, 1996) or No-U Turn Sampling (Hoffman and Gelman, 2014), emulator-based sampling will provide denser samples and more fully resolved posterior distributions than using GlaDS directly for any of these sampling strategies. While it seems that some of the bias in posterior modes (e.g. Figs. 4, S14 and S15) may be partly a result of emulator error, this bias seems to be an appropriate trade-off for such a significant speedup in sampling.

## 6. Discussion

## 6.1. Parameter estimates

The synthetic calibration experiment shows that, even with perfect model–data fit, we do not learn about the true value of all parameters. This limitation arises in part because various parameter combinations produce similar outputs, as evidenced by the pairwise correlations up to  $|r| \geq 0.4$ ), and also because the point-scale flotation fraction is not sensitive to all parameters (e.g. Hill and others, 2025). The slight bias in the most-likely inferred values

might be partially explained by differences between emulator predictions and GlaDS simulations, as evidenced by the reduction in bias associated with including more principal components (Fig. S9) and adding more GlaDS simulations (Fig. S10), both of which reduce emulator prediction error (Fig. S4).

The real borehole time series yields weaker parameter constraints than the synthetic experiment. This is to be expected given the shorter observation period, which does not include the spring event, and the serious model-data discrepancy (e.g. Fig. 7). Despite these limitations, the posterior parameter distributions can guide parameter selection to produce model outputs that are closer to reality than by using uncalibrated values. In the case of the iceflow coefficient, the inferred value  $A \approx 10^{-22} \, \mathrm{Pa}^{-3} \, \mathrm{s}^{-1}$  is outside the range typically suggested for basal ice at the pressure-melting point (e.g. Cuffey and Paterson, 2010) and perhaps points to model shortcomings, limitations in the model setup or discrepancy in the assumed n = 3 stress exponent (e.g. Millstein and others, 2022; Schohn and others, 2025). Other basal characteristics such as the anticipated high water content of basal ice (e.g. macroscopic water content of 2.9-4.6% within temperate basal ice; Brown and others, 2017), anisotropic viscosity of basal ice (e.g. Hofstede and others, 2018) and entrained debris (e.g. Harper and others, 2017) may also contribute to this high A value. For example, Cohen 2000 inferred ice-flow coefficients for simple shear as high as  $A = 1.5 \times$ 10<sup>-22</sup> Pa<sup>-3</sup> s<sup>-1</sup> at Engabreen, Norway, explained as representing enhanced shear as a consequence of bed-parallel unbound water layers laminated between layers of clean and dirty ice. Combined with the influence of unknown, irregular cavity geometries on creep-closure rates (e.g. Helanow and others, 2021), it is not clear where to set a reasonable upper bound for the creep-closure iceflow coefficient.

Of the eight calibration parameters (Table 1), the sheet conductivity  $k_s$ , describing the transmissivity of the drainage system as a whole, the form of bed bumps as described by their height  $h_b$ and aspect ratio  $r_b$ , and the channel conductivity  $k_c$  most directly describe physical aspects of the subglacial drainage system. Other parameters are necessary for the model but describe aspects of the englacial drainage system (englacial storage parameter  $e_y$ ) or basal ice that could be inferred through other means (ice-flow coefficient A), could be constrained by fluid-flow physics (laminarturbulent transition parameter  $\omega$ ), or are model-specific parameters with little physical interpretation (sheet-width below channels  $l_c$ ). The strongest constraints on physical subglacial hydraulic processes, therefore, would come from calibrating parameters in the first group listed above; however, we have obtained the strongest constraint on the ice-flow coefficient A. While the channel conductivity perhaps includes some information about subglacial and englacial conduits (e.g. Pohle and others, 2022), we do not robustly learn about the scale of cavities through  $h_b$  or the transmissivity of the drainage system through  $k_s$  (Figs. 6 and S14). We have learned about  $k_s$  in the synthetic calibration experiment, suggesting that model-data discrepancy, and perhaps the lack of borehole data during the spring, limits our ability to estimate this parameter from the data. In neither case do we learn about the bed bump height  $h_{\rm b}$ , which controls the maximum water depth in subglacial cavities, reinforcing that point-scale water pressure is not sensitive to  $h_{\rm b}$  (e.g. Hill and others, 2025).

The posterior estimates that we have derived based on calibration with the real borehole water-pressure time series differ from those derived by Brinkerhoff and others 2021 based on calibrating parameters of a coupled hydrology–ice-flow model applied to the same region in western Greenland. With a slightly modified

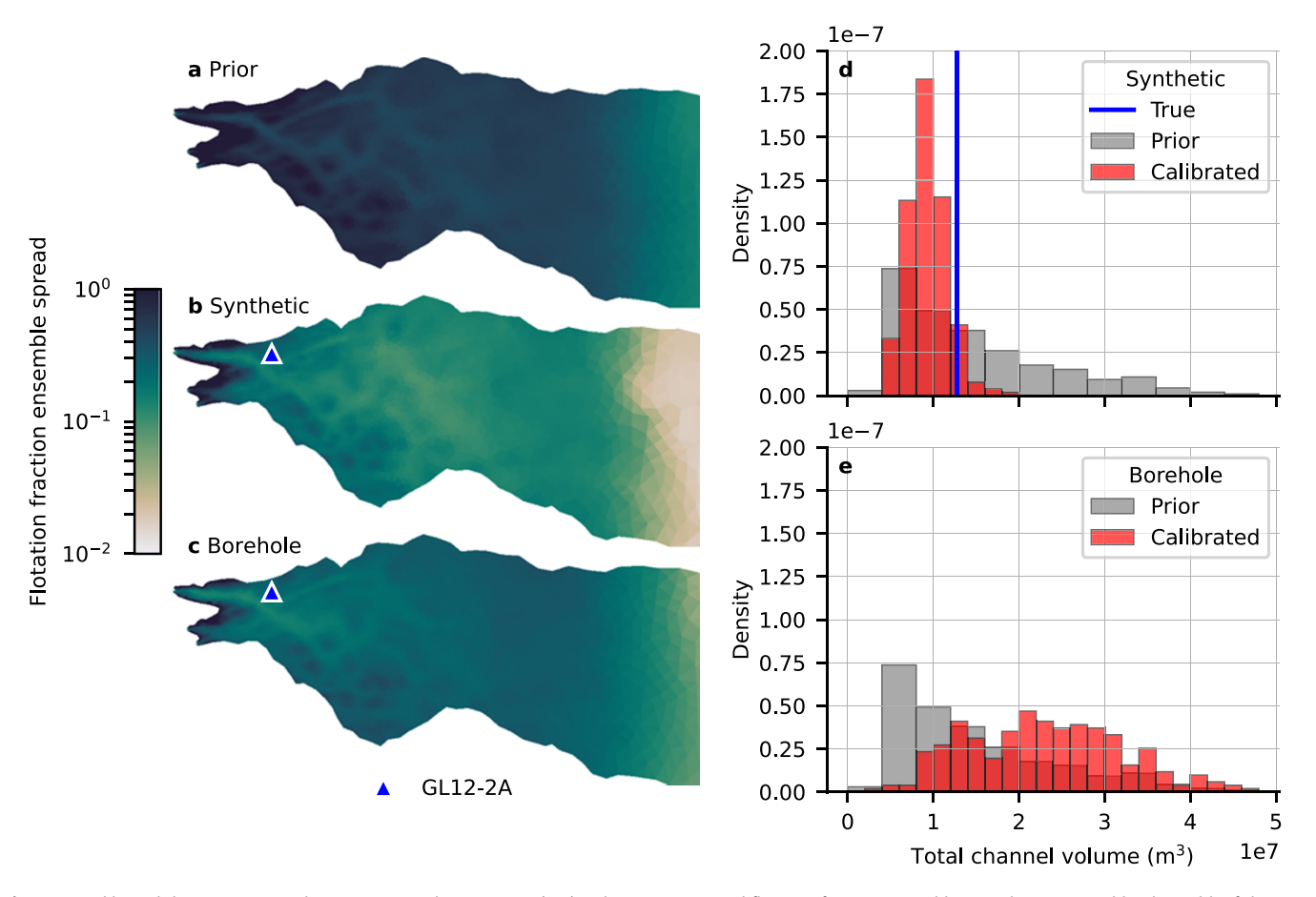
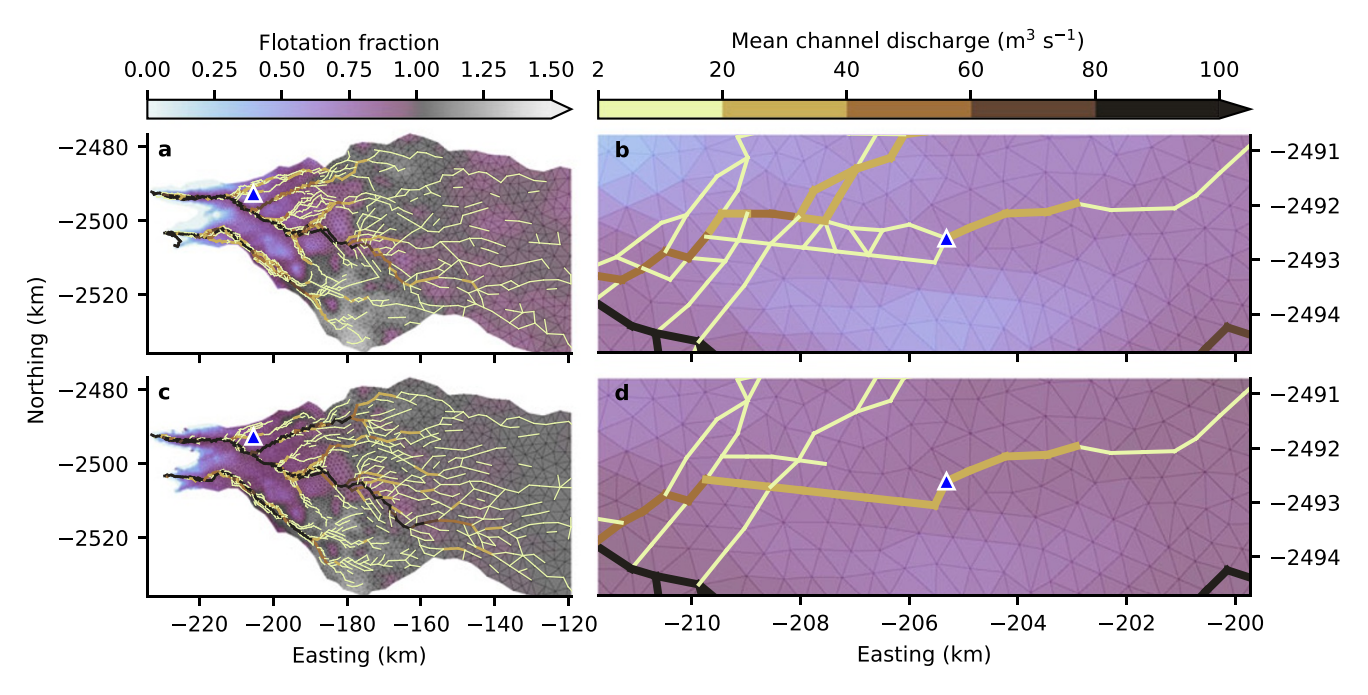


Figure 9. Calibrated drainage system characteristics and uncertainty. (a–c) Melt season-averaged flotation-fraction ensemble spread as measured by the width of the 95% prediction intervals before calibration (a), after calibrating with synthetic observations (b) and after calibrating with borehole observations (c). (d–e) Prior and calibrated domain-integrated channel volume on day 229 (16 August) corresponding to synthetic (d) and borehole (e) observations. The true channel volume in (d) corresponds to the simulation used as synthetic observations.

version of GlaDS as the hydrology model, Brinkerhoff and others 2021 used a neural network emulator to estimate parameter distributions that produce the best fit to satellite-derived annual-average surface velocities. Our study and Brinkerhoff and others 2021 both constrain the most likely channel conductivity  $k_c$ , bed bump aspect ratio  $r_b$ , and to some extent, the englacial storage parameter  $e_v$ . We obtain overlapping estimates with Brinkerhoff and others 2021 for  $r_b$  and  $e_v$ , while our range of inferred  $k_c$  values is two to three orders of magnitude higher. In addition to the parameters that we are able to infer, Brinkerhoff and others 2021 constrain the value of the sheet conductivity  $k_s$  and the bed bump height  $h_b$ . We obtain a strong constraint on the ice-flow coefficient A, which Brinkerhoff and others 2021 did not calibrate. These studies infer different pairwise correlations between subglacial drainage model parameters. Brinkerhoff and others 2021 find correlation r = -0.79 between  $k_s$  and  $h_b$ , while we find a much weaker relationship (r = -0.24). This difference may be a consequence of the different sheet-flow parameterizations or that the values of A that we infer are compensating for model shortcomings that are otherwise taken up by other parameters including  $k_s$  and  $h_b$ . We find a correlation r = 0.31between  $r_{\rm b}$  and  $e_{\rm v}$ , whereas Brinkerhoff and others 2021 report a slightly lower correlation of r = 0.2.

The comparable or stronger parameter constraints obtained by Brinkerhoff and others 2021 suggest that this single borehole

water-pressure time series does not contain more information to constrain the parameters of subglacial drainage models than annual-average surface velocities, despite the impact of the filtering effect of ice flow on estimates based on surface velocities. This conclusion hinges on the discrepancy of the subglacial drainage model compared to the borehole water pressure since we obtain much more informative distributions when we remove the discrepancy by using synthetic model-generated data for calibration (Fig. 4). It is also possible that we would more strongly constrain other parameter values, particularly for parameters correlated with A, if we did not vary A across the ensemble (cf. Brinkerhoff and others, 2021). Stronger constraints may also be obtained with multiple, multi-year borehole water-pressure records that cover the full melt season including the spring speedup and a model that more closely matches the measured time series (e.g. Andrews and others, 2014; Ryser and others, 2014; Hoffman and others, 2016). With multiple multi-year borehole time series, it could also be worthwhile to repeat the separate summer-winter calibration experiment (Fig. 8) to reassess whether the results support seasonally varying parameter values (e.g. Downs and others, 2018). Combining both surface-velocity observations and borehole water-pressure data into a single calibration exercise could also provide stronger parameter estimates and further reduce prediction uncertainty.



**Figure 10.** Posterior channel network constraints. Mean channel discharge (using a minimum channel threshold  $Q \ge 2\,\mathrm{m}^3\,\mathrm{s}^{-1}$ ) on day 229 (16 August) for the area below 1850 m (left column) and near the borehole (right column) from the prior ensemble (top row) and after calibrating with borehole observations (bottom row). Mean flotation fraction for the corresponding ensembles is shown for context.

**Table 3.** Computation time corresponding to each step in the study. Computations were timed on AMD Rome 7532 CPUs on the Digital Research Alliance of Canada Narval cluster

Task	CPU time (dd-HH:MM:ss)
Single GlaDS simulation	08:45:00
GlaDS ensemble	187-00:00:00
MCMC sampling	06:33:06-07:55:08
Likelihood evaluation	00:00:4.7-00:00:5.7
Emulator prediction	00:00:17
Calibrated GlaDS ensemble	93-00:00:00
Emulator prediction	00:00:17

# 6.2. Calibrated predictions and drainage-system characteristics

Using a single point-scale flotation-fraction time series, we have reduced the uncertainty in modelled flotation fraction and the configuration of subglacial channels by at least a factor of three in both synthetic and borehole experiments. Uncertainty reduction is appealing from a modelling perspective, however, it is concerning from the view of realistic subglacial drainage. Borehole records such as the one we have used to calibrate the model show pressure gradients as steep as 10 kPa m<sup>-1</sup> between boreholes separated by tens of meters (e.g. Ryser and others, 2014; Wright and others, 2016) and hydraulic connectivity that varies over similar length scales (e.g. Wright and others, 2016; Rada Giacaman and Schoof, 2023). The lack of representation of this basal heterogeneity in models (cf. Hoffman and others, 2016) results in unrealistically high confidence in inferred parameter values and calibrated predictions. The extent of overconfidence could be assessed by repeating the inference with multiple water-pressure time series from nearby boreholes that intersect hydraulically connected drainage if such data were available. For other model limitations, it is more challenging to assess how deficiencies in the theory underpinning models impacts uncertainty in the calibrated model (Section 6.4)

## 6.3. Modelling limitations and challenges

We have made numerous choices in setting up the subglacial drainage model, for instance forbidding cavities from opening by viscous creep, using the laminar-turbulent sheet-flow model (Hill and others, 2024), and using satellite-mapped moulin positions rather than transferring surface melt directly to the bed at each node. It would be possible to include the effect of these choices in the calibration by encoding them as categorical variables. We have instead opted to use the most physically justified option in each case and infer the corresponding parameter values conditioned on the model configuration.

For cavity creep opening, we argue that disallowing opening by viscous creep is the more physically realistic choice because of the disparate timescales between slow creep-opening (days to weeks) and the timescale corresponding to subglacial overpressurization (hours to days) along with the associated unmodelled processes (e.g. hydrofracture, Das and others, 2008; Tsai and Rice, 2010). Furthermore, allowing cavity creep-opening results in extensive regions (e.g. tens of kilometres inland along bed troughs) with sheet thicknesses exceeding the bed bump height for much of the melt season and effectively forming a subglacial lake. We have used the most realistic meltwater inputs reasonably possible at daily resolution, using moulins mapped from Landsat imagery (Yang and Smith, 2016) and surface runoff outputs from the RACMO2.3p2 model (Noël and others, 2018). The laminar-turbulent sheet-flow model is consistent with the well-understood physics of potential gradient-driven flow and produces improved winter water pressures relative to a turbulent-only model (Hill and others, 2024).

Based on sensitivity tests, modelled water pressure at the borehole location is sensitive to the above modelling choices (Fig. S17). Despite efforts to produce a realistic, data-informed model setup, using a simpler, less realistic model results in a better fit to the borehole data in the case of cavity creep-opening and the moulin configuration (Fig. S18), although the single borehole record used

here does not provide enough data to assess these modelling choices more generally. For meltwater inputs through moulins, it is possible that we are missing additional moulins that are fed by streams that are too small to be resolved in the 15 m-resolution Landsat imagery (Yang and Smith, 2016). If this is the case, then a denser moulin configuration may result in model outputs closer to those obtained by transferring surface melt to the bed at every node, while being more realistic. The paradox that using more data in the model setup and intentionally choosing, a priori, the most reasonable parameterizations degrades model performance highlights the challenge of modelling subglacial drainage with the current generation of models and input data. It remains possible that two-way coupling with an ice-flow model which captures hydrology-sliding feedbacks could improve model outputs by reducing the amplitude of pressure variations and increasing winter water pressure (e.g. Hoffman and Price, 2014).

The discrepancy in spatial footprints of the observations and the model makes it difficult to determine which node should be used as the most representative of the borehole observations. For the numerical mesh used here, there are three nodes similarly spaced within 386-454 m of the borehole (Fig. S1). We have chosen to use a node located in the centre of the trough that most consistently has a modelled subglacial channel passing through it (Fig. 10). Since water pressure sometimes varies between these three similarly distant nodes (Fig. S2), it would be best practice for future calibration studies to refine the model mesh around the location of any observations, consider forcing the mesh to have a node at the precise location of the borehole, and to evaluate the sensitivity of the calibration results to the node being used for calibration, considering the possibility of errors in bed elevation. Ideally, multiple borehole time series co-located within the same mesh element could be averaged to upscale the observations. However, the expense of drilling and the high likelihood of intersecting hydraulically isolated bed patches with any given borehole make it rare to find multiple co-located boreholes suitable for comparison with continuum models. Instead, complementary data such as proglacial discharge estimates tracer transit times and concentrations could be used in a multi-stage Bayesian calibration (e.g. Aschwanden and Brinkerhoff, 2022) to provide additional constraints on the drainage model.

## 6.4. Perspectives on subglacial drainage models

The discrepancy between the subglacial drainage model and reality (Fig. 7), and the finding that model predictions are made worse by including more physical insight when making model choices and using real data in the model configuration (Figs S17 and S18), suggests that we should ask: is the subglacial drainage model a useful representation of borehole water pressure? From the perspective of model-data misfit, the model is less useful than simply averaging the observations to obtain a single mean value of water pressure over time. In other words, the model does not effectively reproduce observed variations in borehole water pressure for any parameter values that we have tested. This conclusion does not even consider the behaviour of the model in the spring, when modelled pressure exceeds 150% of overburden for at least several days over a large portion of the domain, violating basic vertical force balance. It does not appear that the model-data misfit will improve with additional data to constrain it, since the misfit appears to be at least partially related to fundamental model shortcomings, rather than arising from residual parameter uncertainty which could plausibly be reduced by additional measurements.

Should the goal of subglacial drainage modelling be to precisely match individual borehole water-pressure time series? Borehole observations characteristically exhibit variability in baseline water pressure and the response to melt forcing over spatial scales of tens of meters or less (e.g. Murray and Clarke, 1995; Ryser and others, 2014; Wright and others, 2016). Considering that ice flow is sensitive to basal conditions averaged over scales of several ice thicknesses (e.g. Kamb and Echelmeyer, 1986), this does not seem like a productive goal for the purpose of explaining and predicting variations in sliding rates, which is the most common motivation for subglacial drainage model development. Instead, a more approachable goal would be to match the average features observed in multiple boreholes, intersecting both hydraulically isolated and connected drainage, within a spatial footprint of several ice-thicknesses.

These conclusions put modellers in a challenging position. It is well-understood that surface melt-forced variations in subglacial drainage influence glacier (e.g. Iken and Bindschadler, 1986) and ice-sheet dynamics (e.g. Joughin and others, 2008; Bartholomew and others, 2010; Palmer and others, 2011). However, our application of a popular subglacial drainage model suggests that it cannot reasonably reproduce direct measurements of subglacial drainage, even when calibrated with real data and parametric uncertainties are accounted for. We suggest that a productive path forward is to re-examine the overall structure of subglacial hydrology models, for instance englacial storage, processes associated with pressures exceeding overburden (e.g. Tsai and Rice, 2010; Schoof and others, 2012), two-way hydrology-sliding feedbacks (e.g. Hoffman and Price, 2014), the form of the relationship between hydrology and basal friction (e.g. Gilbert and others, 2022) and heterogeneous hydraulic connectivity (Hoffman and others, 2016), to improve model behaviour on appropriate spatial and temporal scales. Concurrently, ice-flow models could adopt effectivepressure parameterizations that are consistent with observed borehole water pressures, e.g. effective pressure N = 5-20% of overburden (e.g. Wright and others, 2016) until such subglacial drainage models are developed.

#### 7. Conclusions

We have applied an emulator-based Bayesian calibration method to enable efficient Bayesian inference of parameters of the GlaDS subglacial hydrology model (Werder and others, 2013) given time series observations of flotation fraction (i.e. water pressure relative to ice overburden) at daily resolution. Using borehole water-pressure data from western Greenland, we obtain meaningful constraints on the channel conductivity  $k_{\rm c}$ , bed bump height  $r_{\rm b}$ , ice-flow coefficient A and englacial storage parameter  $e_{\rm v}$ , with correspondingly reduced uncertainty in modelled water pressure. Relative to the uncalibrated model, we have constrained the configuration of subglacial channels near the borehole and, to a lesser degree, across the entire catchment.

The calibrated water-pressure time series overlaps with the overall range of water pressure observed in the borehole, but the calibrated predictions fail to match observed surface melt-forced water-pressure variations. We have shown that this discrepancy between modelled subglacial drainage and borehole observations is not a result of the choice of model parameters, but is rather a structural feature of the model and therefore is unlikely to be reduced by integrating additional field data. While it is unreasonable to expect a spatially distributed continuum model to precisely predict point-scale (i.e. borehole) water-pressure

variations, the structural discrepancy suggests that the limitations of physics-based drainage models, rather than parameter uncertainty or their computational cost, are a rate-limiting step in predicting hydraulically-forced seasonal ice-flow variations.

**Supplementary material.** The supplementary material for this article can be found at https://doi.org/10.1017/aog.2025.10016.

Data availability statement. Code for running GlaDS experiments and calibrating the drainage model, GlaDS model outputs and MCMC samples are available at https://doi.org/10.5281/zenodo.15412093 (Hill and others, 2025b). Surface elevation and ice thickness data are from https://doi.org/10.5067/GMEVBWFLWA7X (Morlighem and others, 2022). The SEPIA package v1.1 (Gattiker and others, 2020), used for emulator-based Bayesian inference, is available at https://github.com/lanl/SEPIA/. The Ice-sheet and Sea-level System Model (ISSM) used for GlaDS simulations is available at https://issm.jpl.nasa.gov/ (Larour and others, 2012). Borehole water-pressure data are available at https://doi.org/10.18739/A20C4SM8X (Harper and Humphrey, 2010-2014). Daily surface runoff outputs from the 5.5 km-resolution RACMO2.3p2 model are available by contacting the Institute for Marine and Atmospheric Research Utrecht

Acknowledgements. TH was supported by Simon Fraser University and the Natural Sciences and Engineering Research Council of Canada (NSERC) Canada Graduate Scholarship program. GF and DB received support from the NSERC Discovery Grants program. This material is based upon work supported by the U.S. Department of Energy, Office of Science, Office of Biological and Environment Research and Office of Advanced Scientific Computing Research under Triad National Security, LLC ('Triad') contract grant 89233218CNA000001 [FWP: LANLF2C2]. This research was enabled in part by support provided by WestDRI (https://training.westdri.ca), Calcul Quebec (https://www.calculquebec.ca/) and the Digital Research Alliance of Canada (https://alliancecan.ca). RACMO2.3p2 model outputs were kindly provided by Christiaan van Dalum. We would like to thank Joel Harper for helpful discussions and for providing borehole data, and Martin Lüthi and an anonymous reviewer for comments on an earlier version of this manuscript.

**Author contributions.** GF, TH and MH conceived of the idea of constraining subglacial drainage model parameters with water-pressure time series. TH and DB contributed to the emulator and calibration methodology with input from MH. TH, GF and MH constructed the subglacial drainage model setup. TH developed and ran the code and visualized the outputs. TH led the manuscript preparation with contributions from GF, DB and MH. All authors interpreted the calibration results and edited the manuscript.

#### **References**

- Andrews LC and 7 others (2014) Direct observations of evolving subglacial drainage beneath the Greenland ice sheet. *Nature* 514(7520), 80–83. doi:10.1038/nature13796
- Aschwanden A and Brinkerhoff D (2022) Calibrated mass loss predictions for the Greenland ice sheet. Geophysical Research Letters 49(19), e2022GL099058. doi:10.1029/2022GL099058
- Bartholomew I, Nienow P, Mair D, Hubbard A, King M and Sole A (2010) Seasonal evolution of subglacial drainage and acceleration in a Greenland outlet glacier. *Nature Geoscience* 3, 408–4011. doi:10.1038/ngeo863
- Bartholomew I, Nienow P, Sole A, Mair D, Cowton T, Palmer S and Wadham J (2011) Supraglacial forcing of subglacial drainage in the ablation zone of the Greenland ice sheet. *Geophysical Research Letters* 38, L08502. doi:10.1029/2011GL047063
- Besag J (1994) Discussion of the Paper by Grenander and Miller. Journal of the Royal Statistical Society: Series B (Methodological) 56(4), 591–592. doi:10.1111/j.2517-6161.1994.tb02001.x
- Brinkerhoff D, Aschwanden A and Fahnestock M (2021) Constraining subglacial processes from surface velocity observations using surrogate-based Bayesian inference. *Journal of Glaciology* **67**(263), 385–403. doi:10.1017/jog. 2020.112

Brown J, Harper J and Humphrey N (2017) Liquid water content in ice estimated through a full-depth ground radar profile and borehole measurements in western Greenland. *The Cryosphere* 11(1), 669–679. doi:10.5194/tc-11-669-2017

- Cohen D (2000) Rheology of ice at the bed of Engabreen, Norway. *Journal of Glaciology* **46**(155), 611–621. doi:10.3189/172756500781832620
- Cook SJ, Christoffersen P, Todd J, Slater D and Chauché N (2020) Coupled modelling of subglacial hydrology and calving-front melting at Store Glacier, West Greenland. The Cryosphere 14(3), 905–924. doi:10.5194/tc-14-905-2020
- Cuffey KM and Paterson WSB (2010) The Physics of Glaciers 4 edn, Amsterdam: Academic Press.
- Das SB, Joughin I, Behn MD, Howat IM, King MA, Lizarralde D and Bhatia MP (2008) Fracture propagation to the base of the Greenland ice sheet during supraglacial lake drainage. *Science* **320**(5877), 778–781. doi:10.1126/science.1153360
- Derkacheva A, Gillet-Chaulet F, Mouginot J, Jager E, Maier N and Cook S (2021) Seasonal evolution of basal environment conditions of Russell sector, West Greenland, inverted from satellite observation of surface flow. *The Cryosphere* 15(12), 5675–5704. doi:10.5194/tc-15-5675-2021
- **Dow CF** (2022) The role of subglacial hydrology in Antarctic ice sheet dynamics and stability: a modelling perspective. *Annals of Glaciology* **63**(87–89), 49–54. doi:10.1017/aog.2023.9
- Dow C, McCormack F, Young D, Greenbaum J, Roberts J and Blankenship D (2020) Totten Glacier subglacial hydrology determined from geophysics and modeling. *Earth and Planetary Science Letters* **531**, 115961. doi:10.1016/j.epsl.2019.115961
- Downs J, Brinkerhoff D and Morlighem M (2023) Inferring time-dependent calving dynamics at Helheim Glacier. *Journal of Glaciology* 69(274), 381–396. doi:10.1017/jog.2022.68
- Downs JZ, Johnson JV, Harper JT, Meierbachtol T and Werder MA (2018)

  Dynamic hydraulic conductivity reconciles mismatch between modeled and observed winter subglacial water pressure. *Journal of Geophysical Research:*Earth Surface 123(4), 818–836. doi:10.1002/2017JF004522
- Ehrenfeucht S, Morlighem M, Rignot E, Dow CF and Mouginot J (2023) Seasonal acceleration of Petermann Glacier, Greenland, from changes in subglacial hydrology. *Geophysical Research Letters* **50**(1), e2022GL098009. doi:10.1029/2022GL098009
- **Gagliardini O and Werder MA** (2018) Influence of increasing surface melt over decadal timescales on land-terminating Greenland-type outlet glaciers. *Journal of Glaciology* **64**(247), 700–710. doi:10.1017/jog.2018.59
- Gattiker J, Klein N, Hutchings G and Lawrence E (2020) lanl/SEPIA: v1.1. Zenodo. doi:10.5281/zenodo.4048801
- Gelman A, Carlin J, Stern H, Dunson D, Vehtari A and Rubin D (2013) 3rd Bayesian Data analysis, New York: Chapman and Hall/CRC.
- Gilbert A, Gimbert F, Thøgersen K, Schuler TV and Kääb A (2022) A consistent framework for coupling basal friction with subglacial hydrology on hard-bedded glaciers. *Geophysical Research Letters* 49(13), e2021GL097507. doi:10.1029/2021GL097507
- Hager AO, Hoffman MJ, Price SF and Schroeder DM (2022) Persistent, extensive channelized drainage modeled beneath Thwaites Glacier, West Antarctica. The Cryosphere 16(9), 3575–3599. doi:10.5194/tc-16-3575-2022
- Harper J and Humphrey N (2010-2014) Basal Water Pressure Measured in 14 boreholes, Isunnguata Sermia Basin, Greenland Ice Sheet, Arctic Data Center. doi:10.18739/A20C4SM8X
- Harper J, Meierbachtol T, Humphrey N, Saito J and Stansberry A (2021) Generation and fate of basal meltwater during winter, western Greenland ice sheet. *The Cryosphere* 15(12), 5409–5421. doi:10.5194/tc-15-5409-2021
- Harper JT, Humphrey NF, Meierbachtol TW, Graly JA and Fischer UH (2017) Borehole measurements indicate hard bed conditions, Kangerlussuaq sector, western Greenland ice sheet. *Journal of Geophysical Research: Earth Surface* 122(9), 1605–1618. doi:10.1002/2017JF004201
- **Helanow C, Iverson NR, Woodard JB and Zoet LK** (2021) A slip law for hard-bedded glaciers derived from observed bed topography. *Science Advances* 7(20), eabe7798. doi:10.1126/sciadv.abe7798
- **Hepburn AJ and 7 others** (2024) The organization of subglacial drainage during the demise of the Finnish Lake District Ice Lobe. *The Cryosphere* **18**(10), 4873–4916. doi:10.5194/tc-18-4873-2024

- Higdon D, Gattiker J, Williams B and Rightley M (2008) Computer model calibration using high-dimensional output. *Journal of the American Statistical Association* 103(482), 570–583. doi:10.1198/016214507000000888
- Higdon D, Kennedy M, Cavendish JC, Cafeo JA and Ryne RD (2004) Combining field data and computer simulations for calibration and prediction. SIAM Journal on Scientific Computing 26(2), 448–466. doi:10.1137/ S1064827503426693
- Hill T, Bingham D, Flowers GE and Hoffman MJ (2025) Computationally efficient subglacial drainage modeling with gaussian process emulation: GlaDS-GP v1.0. Geoscientific Model Development 18, 4045–4074. doi:10. 5194/gmd-18-4045-2025
- Hill T, Flowers GE, Bingham D and Hoffman MJ (2025b) Zenodo. timghill/glads-borehole-calibration. doi:10.5281/zenodo.15412093
- Hill T, Flowers GE, Hoffman MJ, Bingham D and Werder MA (2024) Improved representation of laminar and turbulent sheet flow in subglacial drainage models. *Journal of Glaciology* 70, e24. doi:10.1017/jog.2023.103
- **Hoffman MD and Gelman A** (2014) The No-U-Turn Sampler: Adaptively setting path lengths in Hamiltonian Monte Carlo. *Jornal of Machine Learning Research* **15**(1), 1593–1623.
- Hoffman MJ and 9 others (2016) Greenland subglacial drainage evolution regulated by weakly connected regions of the bed. *Nature communications* 7(1), 13903. doi:10.1038/ncomms13903
- Hoffman MJ and Price S (2014) Feedbacks between coupled subglacial hydrology and glacier dynamics. *Journal of Geophysical Research: Earth Surface* 119(3), 414–436. doi:10.1002/2013JF002943
- **Hofstede C and 7 others** (2018) Physical conditions of fast glacier flow: 2. variable extent of anisotropic ice and soft basal sediment from seismic reflection data acquired on Store Glacier, west Greenland. *Journal of Geophysical Research: Earth Surface* **123**(2), 349–362. doi:10.1002/2017JF004297
- Iken A and Bindschadler RA (1986) Combined measurements of sub-glacial water pressure and surface velocity of Findelengletscher, Switzerland: Conclusions about drainage system and sliding mechanism. Journal of Glaciology 32(110), 101–119. doi:10.3189/S0022143000 006936
- Irarrazaval I, Werder MA, Huss M, Herman F and Mariethoz G (2021)
  Determining the evolution of an alpine glacier drainage system by solving inverse problems. *Journal of Glaciology* 67(263), 421–434. doi:10.1017/jog. 2020.116
- Irarrazaval I, Werder MA, Linde N, Irving J, Herman F and Mariethoz G (2019) Bayesian inference of subglacial channel structures from water pressure and tracer-transit time data: A numerical study based on a 2-D geostatistical modeling approach. *Journal of Geophysical Research: Earth Surface* 124(6), 1625–1644. doi:10.1029/2018JF004921
- Joughin I, Das SB, King MA, Smith BE, Howat IM and Moon T (2008) Seasonal speedup along the western flank of the Greenland ice sheet. Science 320(5877), 781–783. doi:10.1126/science.1153288
- Joughin I, Smith BE and Howat IM (2018) A complete map of Greenland ice velocity derived from satellite data collected over 20 years. *Journal of Glaciology* 64(243), 1–11. doi:10.1017/jog.2017.73
- Joughin I, Smith B, Howat I and Scambos T (2016) MEaSURES Multi-year Greenland Ice Sheet Velocity Mosaic Version 1. https://doi.org/10.5067/ QUA5Q9SVMSJG, Accessed 10 June 2024.
- Kamb B and Echelmeyer KA (1986) Stress-gradient coupling in glacier flow:
  I. Longitudinal averaging of the influence of ice thickness and surface slope.
  Journal of Glaciology 32(111), 267–284. doi:10.3189/S0022143000015604
- Kennedy MC and O'Hagan A (2001) Bayesian calibration of computer models. Journal of the Royal Statistical Society: Series B (Statistical Methodology) 63(3), 425–464. doi:10.1111/1467-9868.00294
- Khan SA and 8 others (2024) Inland summer speedup at Zachariæ Isstrøm, northeast Greenland, driven by subglacial hydrology. *Geophysical Research Letters* 51(18), e2024GL110691. doi:10.1029/2024GL110691
- Larour E, Seroussi H, Morlighem M and Rignot E (2012) Continental scale, high order, high spatial resolution, ice sheet modeling using the Ice Sheet System Model (ISSM. *Journal of Geophysical Research: Earth Surface* 117, F01022. doi:10.1029/2011JF002140
- **Lindbäck K and 6 others** (2015) Subglacial water drainage, storage, and piracy beneath the Greenland ice sheet. *Geophysical Research Letters* **42**(18), 7606–7614. doi:10.1002/2015GL065393

Meierbachtol T, Harper J and Humphrey N (2013) Basal drainage system response to increasing surface melt on the Greenland ice sheet. *Science* 341(6147), 777–779. doi:10.1126/science.1235905

- Meierbachtol TW, Harper JT, Humphrey NF and Wright PJ (2016) Mechanical forcing of water pressure in a hydraulically isolated reach beneath Western Greenland's ablation zone. *Annals of Glaciology* 57(72), 62–70. doi:10.1017/aog.2016.5
- Meierbachtol TW, Harper JT, Johnson JV, Humphrey NF and Brinkerhoff DJ (2015) Thermal boundary conditions on western Greenland: Observational constraints and impacts on the modeled thermomechanical state. *Journal of Geophysical Research: Earth Surface* 120(3), 623–636. doi:10.1002/2014JF003375
- Metropolis N, Rosenbluth AW, Rosenbluth MN, Teller AH and Teller E (1953) Equation of State Calculations by Fast Computing Machines. The Journal of Chemical Physics 21(6), 1087–1092. doi:10.1063/1.1699114
- Millstein JD, Minchew BM and Pegler SS (2022) Ice viscosity is more sensitive to stress than commonly assumed. *Communications Earth & Environment* 3(1), 57 doi:10.1038/s43247-022-00385-x
- Morlighem M and 31 others (2017) BedMachine v3: Complete bed topography and ocean bathymetry mapping of Greenland from multibeam echo sounding combined with mass conservation. *Geophysical Research Letters* 44(21), 11,051–11,061. doi:10.1002/2017GL074954
- Morlighem M (2022) IceBridge BedMachine Greenland Version 5. https://doi. org/10.5067/GMEVBWFLWA7X, Accessed 16 May 2024.
- Murray T and Clarke GKC (1995) Black-box modeling of the subglacial water system. *Journal of Geophysical Research: Solid Earth* **100**(B6), 10231–10245. doi:10.1029/95JB00671
- Nanni U, Gimbert F, Roux P and Lecointre A (2021) Observing the subglacial hydrology network and its dynamics with a dense seismic array. Proceedings of the National Academy of Sciences 118(28), e2023757118. doi:10.1073/pnas. 2023757118
- Noël B and 10 others (2018) Modelling the climate and surface mass balance of polar ice sheets using RACMO2 Part 1: Greenland (1958–2016). *The Cryosphere* 12(3), 811–831. doi:10.5194/tc-12-811-2018
- Palmer S, Shepherd A, Nienow P and Joughin I (2011) Seasonal speedup of the Greenland Ice Sheet linked to routing of surface water. Earth and Planetary Science Letters 302(3), 423–428. doi:10.1016/j.jpgl.2010. 12.037
- Pohle A, Werder MA, Gräff D and Farinotti D (2022) Characterising englacial R-channels using artificial moulins. *Journal of Glaciology* 68(271), 879–890. doi:10.1017/jog.2022.4
- Rada Giacaman CA and Schoof C (2023) Channelized, distributed, and disconnected: spatial structure and temporal evolution of the subglacial drainage under a valley glacier in the Yukon. *The Cryosphere* 17(2), 761–787. doi:10.5194/tc-17-761-2023
- **Roberts GO and Tweedie RL** (1996) Exponential convergence of Langevin distributions and their discrete approximations. *Bernoulli* **2**(4), 341–363.
- Röthlisberger H (1972) Water pressure in intra-and subglacial channels. Journal of Glaciology 11(62), 177–203. doi:10.3189/S0022143000022188
- Ryser C and 7 others (2014) Caterpillar-like ice motion in the ablation zone of the Greenland ice sheet. *Journal of Geophysical Research: Earth Surface* 119(10), 2258–2271. doi:10.1002/2013JF003067
- Schohn CM, Iverson NR, Zoet LK, Fowler JR and Morgan-Witts N (2025) Linear-viscous flow of temperate ice. *Science* **387**(6730), 182–185. doi:10.1126/science.adp7708
- Schoof C, Hewitt IJ and Werder MA (2012) Flotation and free surface flow in a model for subglacial drainage. Part 1. Distributed drainage. *Journal of Fluid Mechanics* 702, 126–156. doi:10.1017/jfm.2012.165
- Smeets PC and 8 others (2018) The K-transect in west Greenland: Automatic weather station data (1993–2016). Arctic, Antarctic, and Alpine Research 50(1), S100002. doi:10.1080/15230430.2017.1420954
- Sobol' IM (1967) On the distribution of points in a cube and the approximate evaluation of integrals. *Zhurnal Vychislitelnoi Matematiki i Matematicheskoi* Fiziki 7(4), 784–802.
- Sole A, Nienow P, Bartholomew I, Mair D, Cowton T, Tedstone A and King MA (2013) Winter motion mediates dynamic response of the

Greenland ice sheet to warmer summers. *Geophysical Research Letters* **40**(15), 3940–3944. doi:10.1002/grl.50764

- Sommers AN and 7 others (2024) Velocity of Greenland's Helheim glacier controlled both by terminus effects and subglacial hydrology with distinct realms of influence. *Geophysical Research Letters* 51(15), e2024GL109168. doi:10.1029/2024GL109168
- Tsai VC and Rice JR (2010) A model for turbulent hydraulic fracture and application to crack propagation at glacier beds. *Journal of Geophysical Research: Earth Surface* 115, F03007. doi:10.1029/2009JF001474
- van de Wal RSW and 6 others (2008) Large and rapid melt-induced velocity changes in the ablation zone of the Greenland ice sheet. *Science* 321(5885), 111–113. doi:10.1126/science.1158540
- Verjans V and Robel A (2024) Accelerating subglacial hydrology for ice sheet models with deep learning methods. Geophysical Research Letters 51(2), e2023GL105281. doi:10.1029/2023GL105281
- Wearing MG, Dow CF, Goldberg DN, Gourmelen N, Hogg AE and Jakob L (2024) Characterizing subglacial hydrology within the Amery Ice Shelf

- catchment using numerical modeling and satellite altimetry. *Journal of Geophysical Research: Earth Surface* **129**(4), e2023JF007421. doi:10.1029/2023JF007421
- Werder MA and Funk M (2009) Dye tracing a jökulhlaup: II. testing a jökulhlaup model against flow speeds inferred from measurements. *Journal of Glaciology* 55(193), 899–908. doi:10.3189/002214309790152375
- Werder MA, Hewitt IJ, Schoof CG and Flowers GE (2013) Modeling channelized and distributed subglacial drainage in two dimensions. *Journal of Geophysical Research: Earth Surface* 118(4), 2140–2158. doi:10.1002/jgrf. 20146
- Wright PJ, Harper JT, Humphrey NF and Meierbachtol TW (2016) Measured basal water pressure variability of the western Greenland ice sheet: Implications for hydraulic potential. *Journal of Geophysical Research: Earth Surface* 121(6), 1134–1147. doi:10.1002/2016JF003819
- Yang K and Smith LC (2016) Internally drained catchments dominate supraglacial hydrology of the southwest Greenland ice sheet. *Journal of Geophysical Research: Earth Surface* 121(10), 1891–1910. doi:10.1002/2016JF003927